Numerical simulations of the flow in a converging-diverging channel with control through a spanwise slot.

Guillaume Fournier[1,2], Jean-Philippe Laval[1,2], Caroline Braud[1,2] and Michel Stanislas[1,3]
[1]*CNRS, UMR 8107, F-59650 Villeneuve d'Ascq, France*
[2]*Univ Lille Nord de France, F-59000 Lille, France*
[3]*ECLille, LML, F-59650 Villeneuve d'Ascq, France*

Abstract
The flow in a converging-diverging channel at $Re_\tau = 180$ is studied by Direct Numerical and Large Eddy Simulations. Continuous and pulsed jets are applied normally to the wall through a spanwise slot to delay the separation. The influence of the position is first analysed and it is shown that the control efficiency is closely linked to the location of the actuation within the channel. A parametric study on both the intensity and pulsating frequency for the "optimal" position shows that the separation can be drastically reduced and even vanishes with a proper choice of parameters. It is additionally reported that pulsed jets yield better results than continuous jets at an equivalent mass-flux. Moreover, low frequencies are shown to be more efficient than high frequencies. A physical analysis finally demonstrates that the efficiency of the low frequency pulsed jets is mainly due to the creation of spanwise structures, that does not occur in other cases.

1. INTRODUCTION

Delaying or preventing Turbulent Boundary Layer (TBL) separation is of crucial importance for many engineering applications since this phenomenon is generally associated to a loss of aerodynamic performances (decrease of the lift-to-drag ratio) and significant drawbacks (noise, pollution ...). In order to solve this problem, many studies have been conducted in the last decades for a huge variety of flows, from flat plates to multi-element airfoils and several types of control strategies have been tested [4, 6]. Among them, two control techniques have been widely used:

First, the Vortex Generators (VGs) were shown to be rather effective in reducing and even suppressing the separation [8]. Those actuators are designed in such a way that streamwise vortices are created in their wake in order to increase the turbulence intensities in the boundary layer by entraining high-momentum fluid towards the wall, hence delaying the separation [16]. Those structures are meant to be similar to those around the streaks that can be found in uncontrolled boundary layers, since Lumley has demonstrated that most of the turbulent kinetic energy in the boundary layer is contained in this kind of natural coherent structures [17]. However, as VGs cannot be turned off when not needed (during cruise flight for instance), they were rapidly replaced by on-demand active devices such as Zero-Net Mass Flux (ZNMF) actuators [1, 2, 7] or plasma actuators [21, 22] which can produce continuous and pulsed jets. When individual round jets are inclined relatively to the wall (pitch angle) and to the free-stream velocity (skew angle), they are able to create the same kind of structures. They are referred to as fluidic VGs or Vortex Generator Jets (VGJs).

Besides, the pulsed jets emanating from a spanwise slot into the main flow is often used. Although they are similar to the VGJs in many points, particularly in the range of Velocity Ratios (VRs) and of frequencies that can be used, they fundamentally differ in the physics involved. Indeed, because of the 2D geometry of the slot, spanwise vortices are initially produced. Several studies have shown the control efficiency of such a geometry [3, 5, 23]. Moreover an enhancement of the control efficiency is systematically found using a particular frequency range of the actuator pulsation. This frequency range is generally related to instabilities present in the baseline flow (see e.g. airfoils [10, 23], backward facing steps [5], or humps [3]). In strongly separated flows, the Kelvin-Helmholtz instability, coming

* Corresponding Author: Guillaume.Fournier@iup.univ-evry.fr
† Permanent address: Laboratoire de Mécanique et d'Énergetique d'Évry, 40 Rue du Pelvoux, F-91020 Evry Cedex, FRANCE.

from the separated shear layers is the most receptive [10]. In the present study, the baseline flow configuration is a converging/diverging channel created by a smooth bump on a wall. As discussed in §3, a slight flow separation occurs after the summit. For this configuration, two instabilities are identified: the Kelvin-Helmholtz instability, in the shear layer, and the instability of the streaks recently found by Marquillie *et. al*. [18].

The aim of the present study is to investigate the receptivity of this flow configuration using pulsed actuation through slots and to demonstrate that it is possible, using an efficient jet-based control, to drastically reduce the size of the recirculation bubble, which is of strong interest in the industrial applications.

This paper is divided into six parts. The numerical methods for both Direct Numerical Simulations (DNS) and Large Eddy Simulations (LES) are first given in §2. The baseline flow is then briefly introduced in §3. After a short validation comparison between DNS and LES results in the uncontrolled case, presented in §4, the results of a parametric study on the control location and intensity, obtained by DNS, are discussed in §5. The influence of the frequency and the velocity ratio on the control efficiency is then analysed by means of LES in §6. Finally, a detailed physical analysis is proposed to explain why some frequencies are more efficient than others (§7).

2. NUMERICAL CONSIDERATIONS

The numerical methods used for this study have already been described in detail in [19] so only a brief overview will be given here. The originality of the code used is that instead of solving the Navier-Stokes equations in curvilinear coordinates, a mapping is applied to transform the partial differential operators so that the cartesian coordinates can be used. This technique allows us to have rather complex 2D geometries without having subsequent mesh issues. The equations are integrated in time using an implicit second-order backward Euler scheme. The cartesian part of the laplacian, coming from the mapping, is treated implicitly while other mapping-induced operators and non-linear convective terms are discretised with an explicit second-order Adams-Bashforth scheme. Spatial discretisations in the streamwise direction *(X)* are performed using a fourth-order central-difference scheme for the second derivatives and eighth-order for the first derivatives. Spectral methods are used in both wall-normal (Y) and spanwise (Z) directions with Chebychev-collocation and Fourier expansion, respectively.

The incompressible flow in a converging-diverging channel is computed using both DNS and LES. The computational domain can be found in Figure 1. Its extents are $L_X = 4\pi$, $L_Y = 2$ and $L_Z = 2\pi$ in the streamwise, wall-normal and spanwise directions respectively.

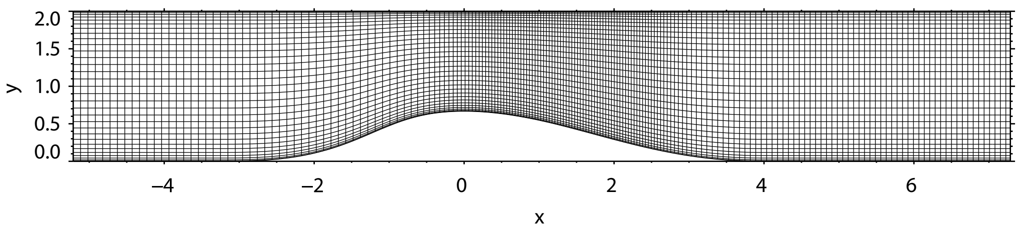

Figure 1: Computational domain used for the present study (DNS). Every 4 mesh points are plotted in each direction.

The lower wall has the same shape as the bump used in the LML wind tunnel for the AEROMEMS 1 & 2 EC projects. This geometry and the flow characteristics at high Reynolds number are detailed by Kostas *et. al*. [12]. As the Reynolds numbers involved in experiments (Re_τ 6, 500) are much larger than those that can be obtained in DNS (up to Re_τ 600), a quantitative comparison between the two approaches would be irrelevant. However the pressure gradient distributions are similar and allow qualitative comparisons if needed. The meshes used, identical for all the cases considered for each numerical method, are $768(X) \times 129(Y) \times 384(Z)$ and $512(X) \times 97(Y) \times 128(Z)$ for DNS and LES, respectively. The cell sizes in wall units are summarised in table 1 at two different locations, corresponding to the inlet and the position of maximum friction velocity ($X = -0.75$). As shown in Figure 1, the mesh is strongly stretched in the streamwise direction so that the LES case is almost fully resolved locally in the streamwise direction, close to the actuator. As a result of a previous LES study [14], the Wall-adapting local eddy-viscosity (WALE) subgrid-scale model [20] was chosen for the LES part of this study.

Table 1: Mesh characteritics for DNS and LES at two different locations, corresponding to the top of the bump (X = 0) and the position of maximum friction velocity (X = –0.75).

Case	Mesh	$\Delta x^+\|_{X=0}$	$\Delta y^+\|_{X=0}$		$\Delta z^+\|_{X=0}$	$\Delta x^+\|_{u_\tau^{max}}$	$\Delta y^+\|_{u_\tau^{max}}$		$\Delta z^+\|_{u_\tau^{max}}$
			Min	Max			Min	Max	
DNS	$768(X) \times 129(Y) \times 384(Z)$	4.6	0.06	4.6	3.1	11.2	0.11	8.7	8.1
LES	$512(X) \times 97(Y) \times 128(Z)$	9.7	0.10	6.1	9.3	4.5	0.19	11.7	24.3

Concerning the boundary conditions, a no-slip condition is applied on both the upper and lower boundaries to simulate solid walls. A classical convective condition $\frac{\partial u_i}{\partial t} + U_c \frac{\partial u_i}{\partial x} = 0$ is used for the outflow plane, with U_c the mean convective velocity at the outlet plane. The time-dependent inlet conditions are taken from a previous DNS of a flat channel flow and the initial field comes from a precursor DNS of the same flow geometry without actuation, both at the same Reynolds number as the present study. Finally, a symmetry condition is applied in the homogeneous spanwise direction.

The actuation is imposed by a velocity distribution on the lower wall over the full span and a short streamwise extent $D_X = 0.09$, corresponding to 16 wall units at the inlet, hence creating an artificial jet through a spanwise slot. The profile of the jet exit velocity U_{jet} through the slot is shown on Figure 2-left. For both numerical and physical reasons, this profile is as smooth as possible both on the edges and at the middle of the slot. In the present study, the jets are normal to the wall. The velocity can also evolve in time (Figure 2-right) in order to mimic pulsed or synthetic jets. The duty cycle $(DC = T_b/T)$, defining the ratio of the blowing duration of the jet T_b over the pulsation period $T = 1/F_j$ (F_j being the control frequency) can be modified independently of the frequency so that the influence of the different phases of a pulsed control can be studied.

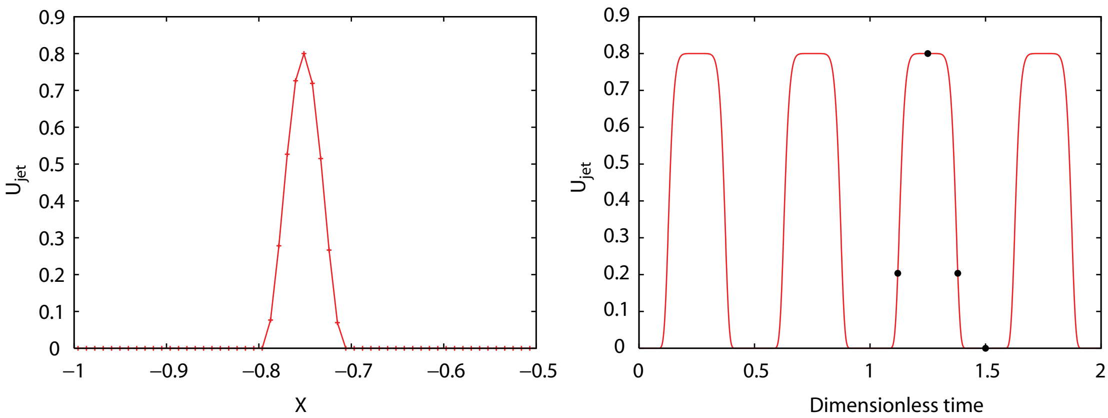

Figure 2: Definition of the actuator. Left: Streamwise distribution of the velocity in the slot; Right: Time evolution of the velocity at the middle of the slot for pulsed jets at F^+ = 6 with DC=50%. The black dots correspond to the time locations used for the phase averages and are, from left to right, $\Phi = \pi/2$, $\Phi = \pi$, $\Phi = 3\pi/2$ and $\Phi = 2\pi$.

In the present study, the flow is integrated over 20 convective time units, based upon the inlet maximum velocity U_∞ and half the channel height h. After a transient, due to the sudden application of the control, the fields are stored every 200 time steps (corresponding to a time duration of 0.2 convective time between two snapshots) for a total of 15 convective time units (1.2 flow-through time) in order to reach the statistical convergence.

3. SHORT DESCRIPTION OF THE BASELINE FLOW

The turbulent flow in a converging-diverging channel at low Reynolds number $Re_\tau = 180$ (based upon the friction velocity at the inlet and half the channel height h) is considered in this study. Because of the shape of the channel, the flow is first subjected to a favourable pressure gradient (FPG), in the converging part. It then encounters a strong adverse pressure gradient (APG) due to the diverging wall (Figure 3-left). Under the influence of both the APG and the low Reynolds number, a large recirculation bubble occurs in the diverging part of the channel, that spreads over ΔX_R 3 (Figure 3-right). The boundary layer thickness at $X = 0$, corresponding to the top of the bump is δ 0.1. The associated displacement and momentum thickness for this position are $\delta^* = 2.5\ 10^{-2}$ and $\theta = 9.9\ 10^{-3}$ respectively.

The vortical structures (Q-criterion) obtained by DNS are displayed in Figure 4. The creation of such structures is obviously enhanced by the presence of the recirculation bubble. In addition, it appears that the flow is also separated on the upper wall of the channel. However, in the following, only the lower curved boundary will be looked at.

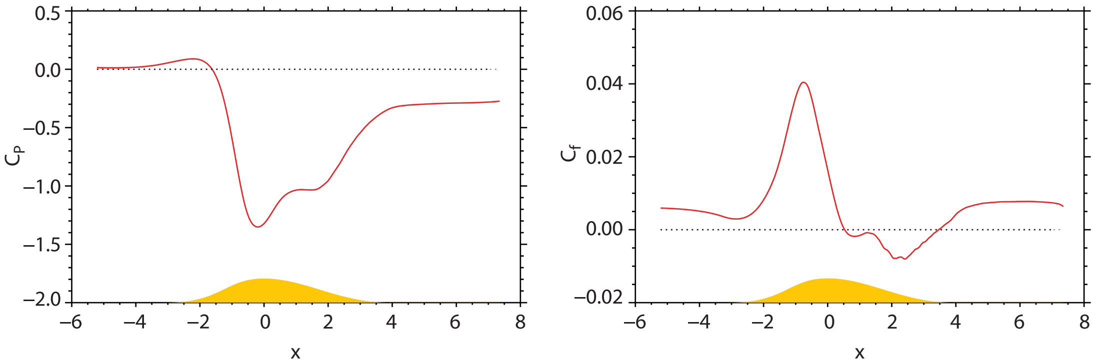

Figure 3: Spanwise-averaged pressure (left) and friction (right) coefficients for the baseline flow. The bump is indicated in yellow.

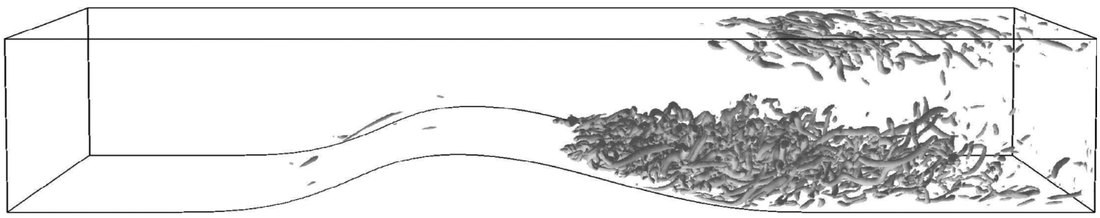

Figure 4: Vortical structures (Q-criterion) obtained by DNS for the baseline flow.

4. COMPARISON BETWEEN DIRECT NUMERICAL AND LARGE EDDY SIMULATIONS

In order to perform a parametric study using LES, it is necessary to know what the differences are between the results obtained by LES and the DNS reference case. As LES will be used in the following for computational time saving, the aim of this section is to validate the LES code. However, for both numerical and mesh differences between the two numerical approaches, it was not possible to accurately validate the LES results for the controlled flow. Therefore, the validation was done in the uncontrolled case, and the conclusions will be extended to the case with control. It is nonetheless noteworthy that a preliminary validation study, performed with two close but different actuations between LES and DNS, showed a fairly good agreement between the two methods.

As shown in Figure 5, the LES results are in very good agreement with DNS in the uncontrolled case. The separation occurs almost at the same position and the bubble has the same shape. Small differences can however be found on the length of the bubble which is about 7% longer when using LES. This statement is confirmed by the streamwise evolution of the friction coefficient (Figure 6).

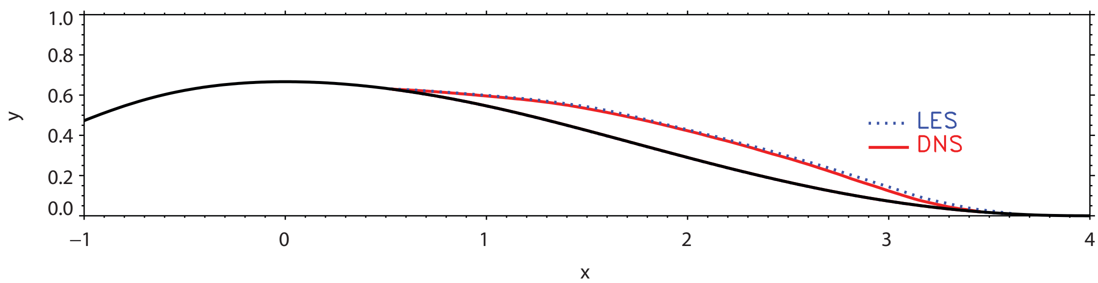

Figure 5: Comparison DNS-LES: comparison of the spanwise-averaged recirculation zones obtained by DNS and LES in the uncontrolled case.

A good agreement between DNS and LES also appears on the wall-normal profiles of the mean streamwise velocity and Reynolds stresses (not shown), for which the DNS and LES data nearly collapse. All these comparisons prove the efficiency of LES in the uncontrolled case, yielding results close to the reference dataset. The interested reader can find a more extensive validation study of LES in [14] for a higher Reynolds number ($Re_\tau = 600$).

In conclusion, it was shown that the results obtained by LES in the uncontrolled case are comparable to the DNS results proving the good ability of LES to predict the flow around the bump. Additionally, a preliminary study demonstrated that a qualitative agreement can be found between LES and DNS in the controlled case, in spite of the slight differences in the actuation. For all those reasons, and provided the number of cases to be considered, LES seems to be the perfect tool for this study that would have been impossible to carry out using DNS.

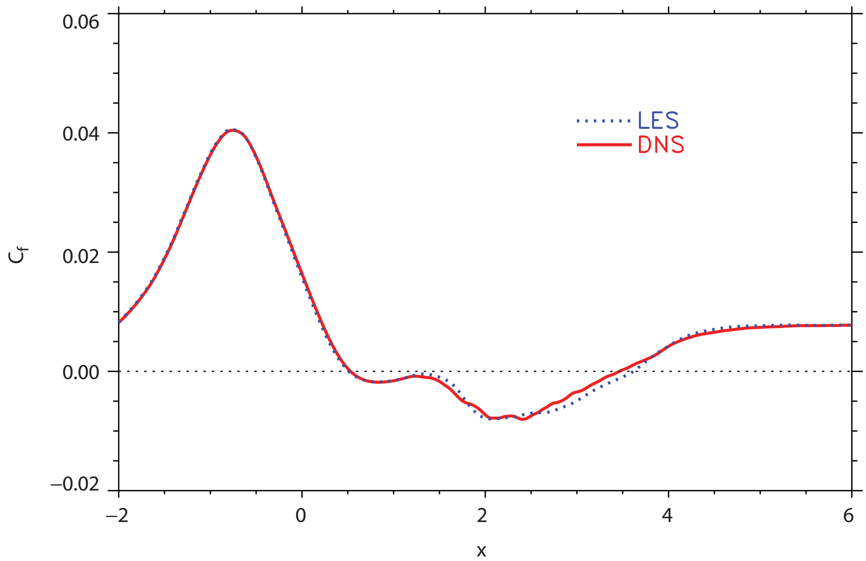

Figure 6: Comparison DNS-LES: streamwise evolution of the spanwise-averaged friction coefficient obtained by DNS and LES in the uncontrolled case.

5. PARAMETRIC STUDY USING DIRECT NUMERICAL SIMULATIONS

The first part of the present study consists in studying the influence of two parameters: the slot location, measured with respect to the top of the bump, and the velocity ratio defined by $VR = U_{jet}^{max}/U_\infty$, U_{jet}^{max} being the maximum velocity at the exit of the slot. The objective of this parametric study was to find, by means of DNS, an efficient control using normal jets that would be considered more thoroughly by LES in a following section.

5.1. Influence of the position on the control efficiency

The influence of the control location is first studied in the continuous mode (DC=1) for a rather small velocity ratio $VR = 0.5$. Three different positions are considered. The first one (S1) is located right after the top of the bump ($X_c = 0.06$) in the adverse pressure gradient region while the second one (S2) is slightly upstream of it ($X_c = -0.13$), where the pressure gradient is favourable. The third position (S3) is located where the boundary layer is the thinnest in the uncontrolled case ($X_c = -0.75$), corresponding to the highest friction coefficient. A summary of the cases considered can be found in Table 2, where D_X^+ stands for the slot width in wall units based on the inlet friction velocity, C_μ is the momentum coefficient defined as in [5]:

$$C\mu = \frac{D_X}{\Delta X_R}\left(\frac{U_{jet}^{\max}}{U\infty}\right)^2$$

and Fl is the ratio between the mass flux coming through the slot and the total mass flux at the inlet of the channel formally defined such as:

$$Fl = \frac{\int_{slot} \vec{V}\,\vec{n}\,dS}{\int_{inlet} \vec{V}\,\vec{n}\,dS}n$$

In the following, each case is named under the form *Num_Sβ_Vγ* where *Num* is either DNS or LES depending on the numerical technique, β represents the slot position and γ, the velocity ratio used.

Table 2: Summary of the DNS test cases.

Case	Position (X_c)	D_X^+	*VR*	$C\mu$	FI
DNS_S1_V0.5	+0.06	17	0.5	0.8%	1.3%
DNS_S2_V0.5	–0.13	20	0.5	0.9%	1.4%
DNS_S3_V0.5	–0.75	16	0.5	0.7%	1.5%
DNS_S3_V0.8	–0.75	16	0.8	1.9%	2.5%

Figures 7 and 8 give the shape of the recirculation bubble and the streamwise evolution of the friction coefficient respectively. As can be seen, the slot location has a strong influence on the control efficiency. Two different behaviours appear. For the first two positions S1 and S2, the boundary layer separates right downstream of the slot, under the influence of the jet. The separation zone then grows and the boundary layer eventually reattaches around the same position as in the uncontrolled case for S2 and farther downstream for S1. As a consequence, these actuator positions are not efficient to reattach the flow. The recirculation zones obtained are between 20% (S2) and 30% (S1) larger compared to the case without actuation. It is also noteworthy that, for these two cases, the maximum height of the separation bubble is significantly increased by the control. The last position tested leads to totally different results. Because of the favourable pressure gradient in the converging part where the slot is located, the separation induced by the jet coming outwards of the slot quickly reattaches. The boundary layer continues to develop until it separates slightly upstream of the reference case and reattaches. The separation bubble obtained is then 20% smaller and half the height of the bubble in the uncontrolled case, proving that the control can be efficient provided it is properly applied. In the following part of this study, only the S3 slot will be characterised.

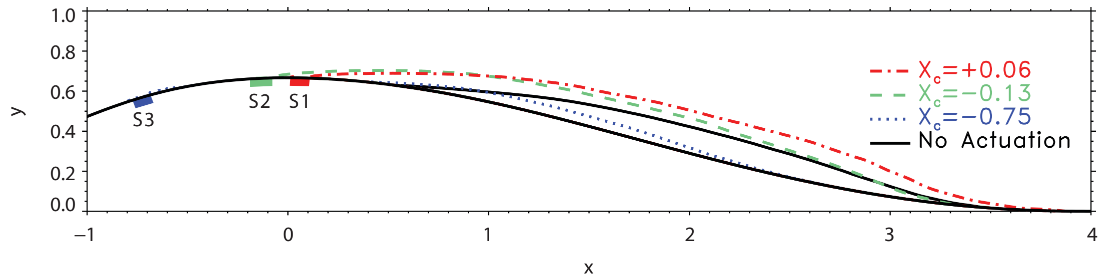

Figure 7: Influence of the slot position: comparison of the spanwise-averaged recirculation zones obtained at *VR* = 0.5 for a control through S1 (X_c = 0.06), S2 (X_c = –0.13) and S3 (X_c = –0.75).

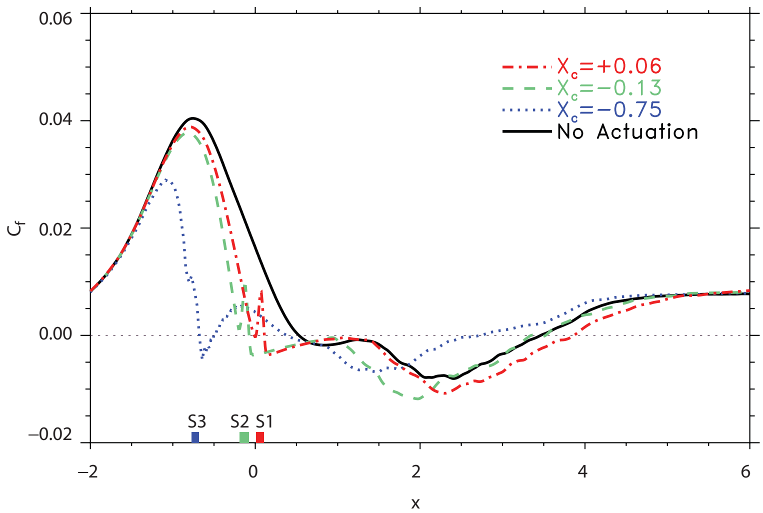

Figure 8: Influence of the slot position: streamwise evolution of the spanwise-averaged friction coefficients obtained at VR = 0.5 for a control through S1 (X_c = 0.06), S2 (X_c = –0.13) and S3 (X_c = –0.75).

5.2. Influence of the velocity ratio

A higher velocity ratio $VR = 0.8$ was then applied at S3 in order to see if the previous results can be further improved. The mean recirculation zones obtained for $VR = 0.5$ and $VR = 0.8$ are compared to the uncontrolled case in Figure 9.

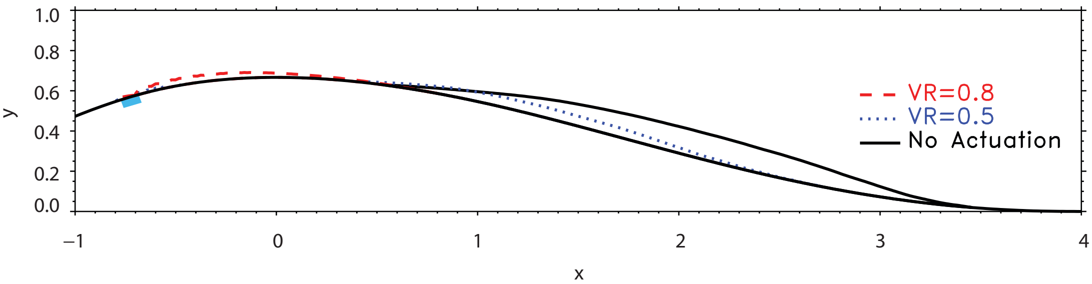

Figure 9: Influence of the control intensity: comparison of the spanwise-averaged recirculation zones obtained for a control through S3 ($X_c = -0.75$) at $VR = 0.5$ and $VR = 0.8$.

Under the effect of a higher jet velocity, a bigger separation bubble occurs downstream of the slot for $VR = 0.8$ which is attributed to the jet's own wake from the observation of the instantaneous field. However, thanks to this recirculation zone, the velocity distribution in the boundary layer is deeply modified and the flow no longer separates in the diverging part of the bump, as it is the case for both $VR = 0.5$ and the uncontrolled case. As the main separation is totally suppressed when using a higher velocity ratio, the DNS_S3_V0.8 case was chosen as a starting point for the next part of the study concerning pulsed jets, presented in §6.

6. PARAMETRIC STUDY USING LES

The second part of this study was aimed at studying the influence of several parameters on the efficiency of the control at S3, mainly by pulsed jets. The influence of the frequency and the velocity ratio was investigated. Additionally, the impact of the velocity ratio in the continuous control case was also considered.

As it was shown earlier in §5, a steady control through S3 is able to drastically reduce the length of the separation zone developing along the diverging part of the bump. However, the mass flow rate involved in such a control is significant. One may expect that the energy cost of the control can be reduced without decreasing its efficiency by using pulsed jets [11, 12, 24]. In addition, many studies in the literature have shown that unsteady actuators can be more efficient than continuous jets [23]. As it can lead to both energy savings and effectiveness improvement, the case of pulsed jets is investigated in the following sections. Moreover, preferential excitation frequencies have been reported to enhance the control efficiency by several authors [5, 10]. All the pulsed cases tested to characterise the frequency influence are summarised in Table 3. In order to consider Strouhal numbers for the actuation and therefore make comparisons with earlier studies, all actuating frequencies are scaled using the inlet maximum velocity U_∞ and the recirculation length in the uncontrolled case ΔX_R so that $F^+ = F_j \, \Delta X_R / U_\infty$. It is noteworthy to recall that the width of the slot is $D_X = 0.09$ (16 wall-units at the inlet) which corresponds roughly to the height of the boundary layer at the top of the bump in the uncontrolled case (δ 0.1).

Table 3: Summary of the LES test cases.

Case	*VR*	*Cμ*	F^+	DC	FI
LES_S3_F0_V4	0.4	0.5%	0	100%	1%
LES_S3_F6_V8	0.8	1.9%	6	50%	1%
LES_S3_F15_V8	0.8	1.9%	15	50%	1%
LES_S3_F30_V8	0.8	1.9%	30	50%	1%
LES_S3_F60_V8	0.8	1.9%	60	50%	1%
LES_S3_F0_V8	0.8	1.9%	0	100%	2%
LES_S3_F6_V16	1.6	7.6%	6	50%	2%
LES_S3_F60_V16	1.6	7.6%	60	50%	2%
LES_S3_F6_V24	2.4	17.1%	6	50%	3%
LES_S3_F0_V16	1.6	7.6%	0	100%	4%

6.1. Influence of the frequency

The frequency at which the flow is controlled is a key parameter that strongly affects the control efficiency. For a control with synthetic jets, and for slightly different geometries such as rounded ramps [5] or bumps [3, 9], it was pointed out that forcing at a frequency close to the natural shedding frequency ($F^+ = 0.57$) can lead to a decrease of the recirculation length up to 60%. In this case, defined as the *vorticity-dominated mode* ($F^+ = 0.5$) by Dandois et *al*. [5] the reduction of the separation length is associated to an increase of the turbulent kinetic energy and of the entrainment in the boundary layer. On the other hand, when the flow is controlled with high-frequency actuators ($F^+ = 4$, *acoustic-dominated mode*), the recirculation zone is increased by around 40%. As the aforementioned study of Dandois *et al*. was performed on a different geometry (rounded ramp), at a 7-times higher Reynolds number, the values of the frequencies are only given as information, and should not be taken as references. In the present study, a wide range of frequencies ranging from $F^+ = 3$ to $F^+ = 60$ was tested and compared to the steady case ($F^+ = 0$). Tests were performed for two mass-fluxes corresponding to approximately 1% and 2% of the incoming mass-flux in the channel respectively (Table 3). In order to keep the same mass-fluxes, the velocity ratio for the steady case has to be reduced by a factor of two with respect to the unsteady case as the Duty Cycle is fixed (DC=0.5) for all the pulsating frequencies.

The influence of the frequency is first analysed for the lower *VR* corresponding to 1% of the incoming flow in the channel. The results are summarised in Figures 10-14. As shown in Figure 10, high- and low-frequency actuations do not have the same impact on the size of the separation bubble. For the highest frequencies ($F^+ \geq 15$), the pulsation does not have any additional effect with respect to the steady blowing. Indeed, the length and height of the bubble are very close in each case (Figure 10-top). In addition, for these frequencies, a separation bubble occurs in the immediate vicinity of the actuator. On the other hand, for a low-frequency forcing at $F^+ = 3$ (not shown) and $F^+ = 6$, the height of the separation bubble is drastically reduced and there is no separation in the near wake of the jets. Moreover, and even if the length of the bubble is almost unchanged with respect to the steady case, the boundary layer is on the verge of reattachment, as shown by the friction coefficient (Figure 11), and only a small additional effort could lead to a fully attached flow.

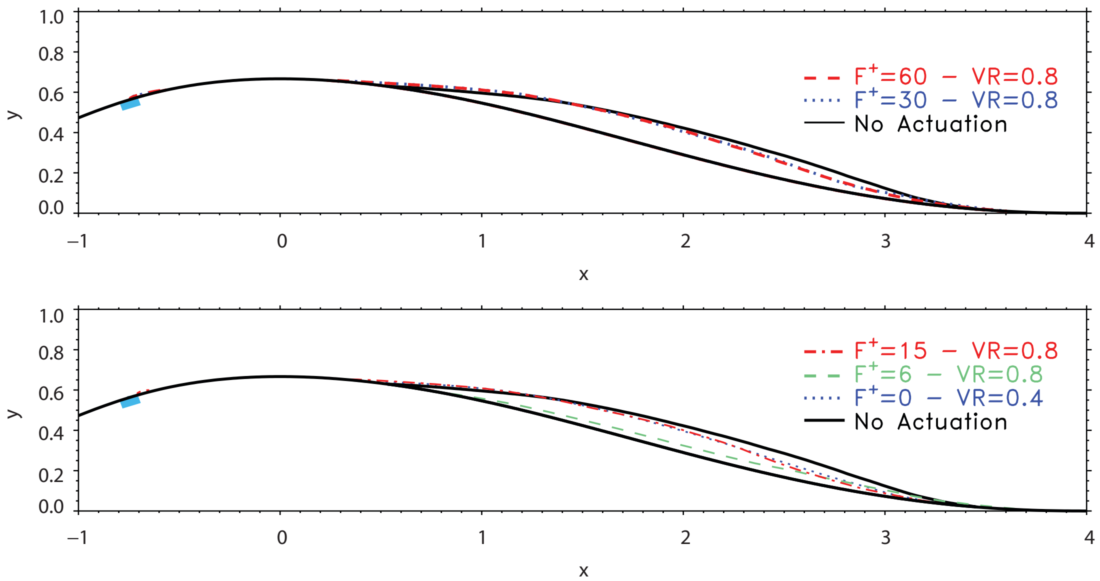

Figure 10: Influence of the frequency: comparison of the spanwise-averaged recirculation zones obtained for a control through S3 with Fl=1%. Top: large frequencies; bottom: small frequencies.

The influence of the frequency is even clearer on the Reynolds-stress profiles (Figures 12-14). At $X = -0.48$ (Figure 12), located less than two slot widths downstream of the actuator, the two opposite effects of the high and low frequency ranges described previously on the recirculation zone clearly appear. For a continuous or a high-frequency actuation, the flow is modified in such a way that the peaks of all the stresses are moved away from the wall, the displacement of $\langle u'u'\rangle$ and $\langle v'v'\rangle$ being larger for the steady case. Compared to the results obtained with $F^+ = 6$, the peak magnitudes of $\langle w'w'\rangle$ and $\langle u'v'\rangle$ are almost unchanged and the general evolution of all stresses are very close between $F^+ = 0$

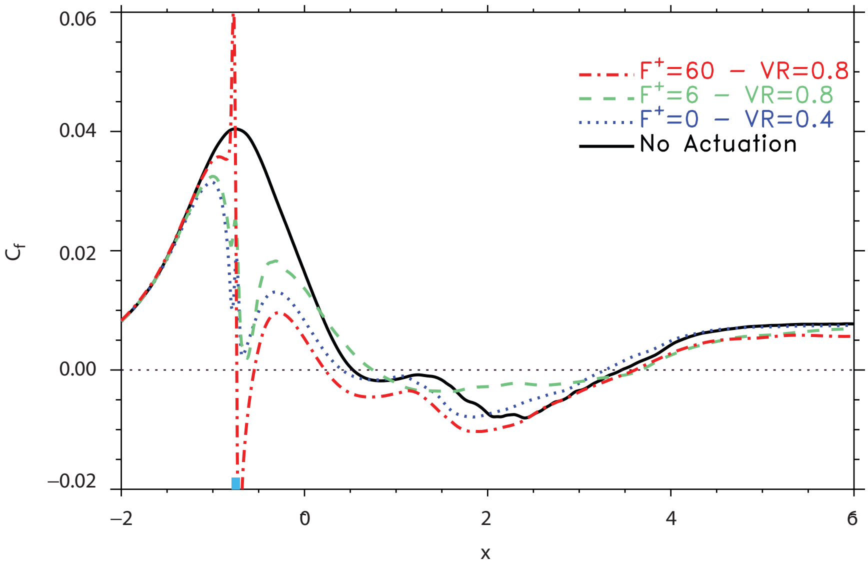

Figure 11: Influence of the frequency: streamwise evolution of the spanwise-averaged friction coefficient obtained for a control through S3 with FI = 1% with three frequencies F^+ = 0, F^+ = 6 and F^+ = 60.

and $F^+ = 60$, proving that high-frequency actuation is comparable to a steady one. A different behaviour of the flow occurs when using a low pulsating frequency. A two-peak pattern is now observed on each stress profile. The first peak corresponds to the one previously observed at the same distance from the wall for both the high-frequency and steady actuation, except on $\langle u'u' \rangle$ for which it is slightly moved away from the wall. A second peak is present closer to the wall. This peak is particularly intense on $\langle u'u' \rangle$ and $\langle v'v' \rangle$ with an amplitude about twice as large as the maximum amplitude of the uncontrolled (and high-frequency) case. This particular pattern is associated to the spanwise vortices which are observed in Figure

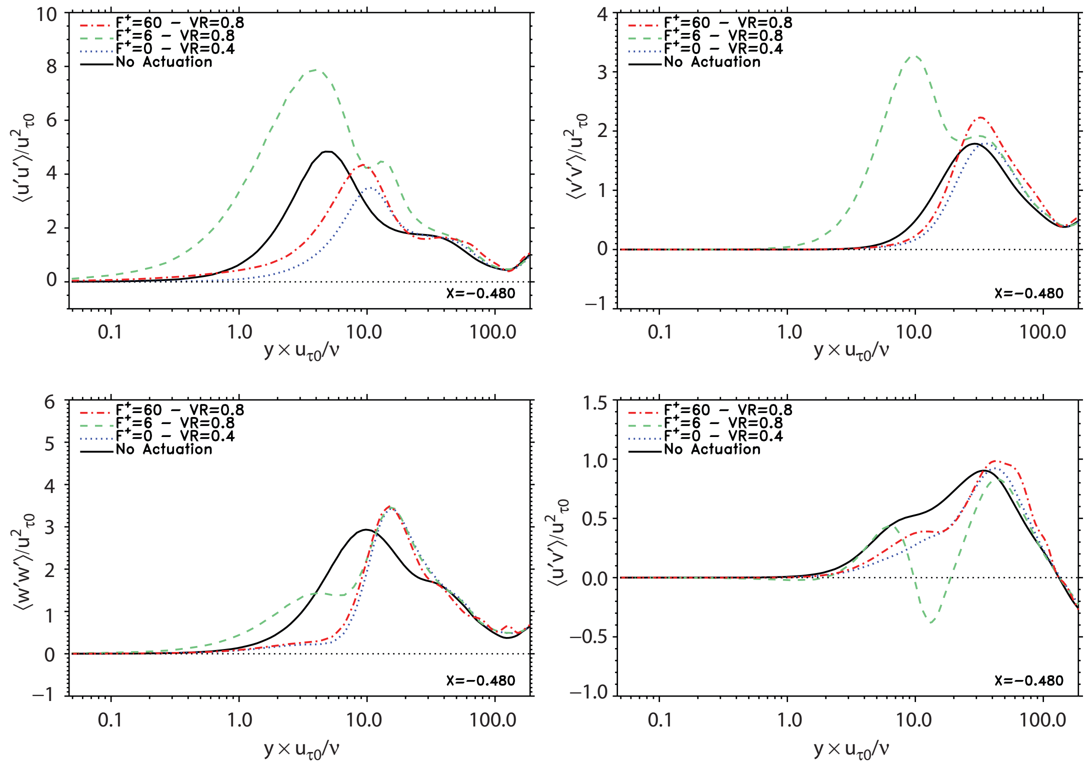

Figure 12: Influence of the frequency: Comparison of the spanwise-averaged Reynolds Stresses at X −0.5, obtained for a control through S3 with FI=1% with three frequencies F + = 0, F + = 6 and F + = 60.

29, only found when using a low pulsating frequency. It is noteworthy that a second peak also appears on $\langle w'w' \rangle$, meaning that, in spite of the 2D character of the control through a spanwise slot, the initially created 2D structures quickly evolve towards 3D vortices. A more detailed phenomenological study will be proposed in §7. However, although all those observations are of high interest, the most remarkable result is found on the shear stress $-\langle u'v' \rangle$. Indeed, additionally to the double-peak pattern, this stress encounters a double change of sign, being positive close to the wall and in the free-stream and becoming negative between y^+ 10 and y^+ 20. This sign inversion is of great interest because the wall-normal derivative of the shear stress is one of the component of the average momentum equation and may explain the fact that the boundary layer is attached in this case [13]. It finally appears that for $F^+ = 6$, the zone of influence of the jet, *i. e.* the zone where non-zero stresses can be found, starts closer to the wall than for a steady or a high-frequency actuation, in the case of the normal stresses.

Farther downstream ($X = 0$), the same observations can be made concerning the continuous and high-frequency actuations (Figure 13). For $F^+ = 60$ and $F^+ = 0$, the peak of Reynolds stresses still appears at slightly higher distances from the wall than in the uncontrolled case. However, the difference of magnitude of those peaks slightly increases from the continuous jets to the pulsed jets at $F^+ = 60$, except on $\langle w'w' \rangle$ where they almost collapse. On the contrary, the stresses obtained for $F^+ = 6$ are quite different from what they were at $X = -0.48$. The double-peak pattern disappears on $\langle u'u' \rangle$ and the intensity of the peak closest to wall is significantly decreased on $\langle v'v' \rangle$. In addition, the shear stress $-\langle u'v' \rangle$ does not change sign anymore and the amplitude of the first peak is increased by more than 100%. The three-dimensionality of the vortices is enhanced with respect to the previous location, which is confirmed by the high level of $\langle w'w' \rangle$ observed throughout the boundary layer.

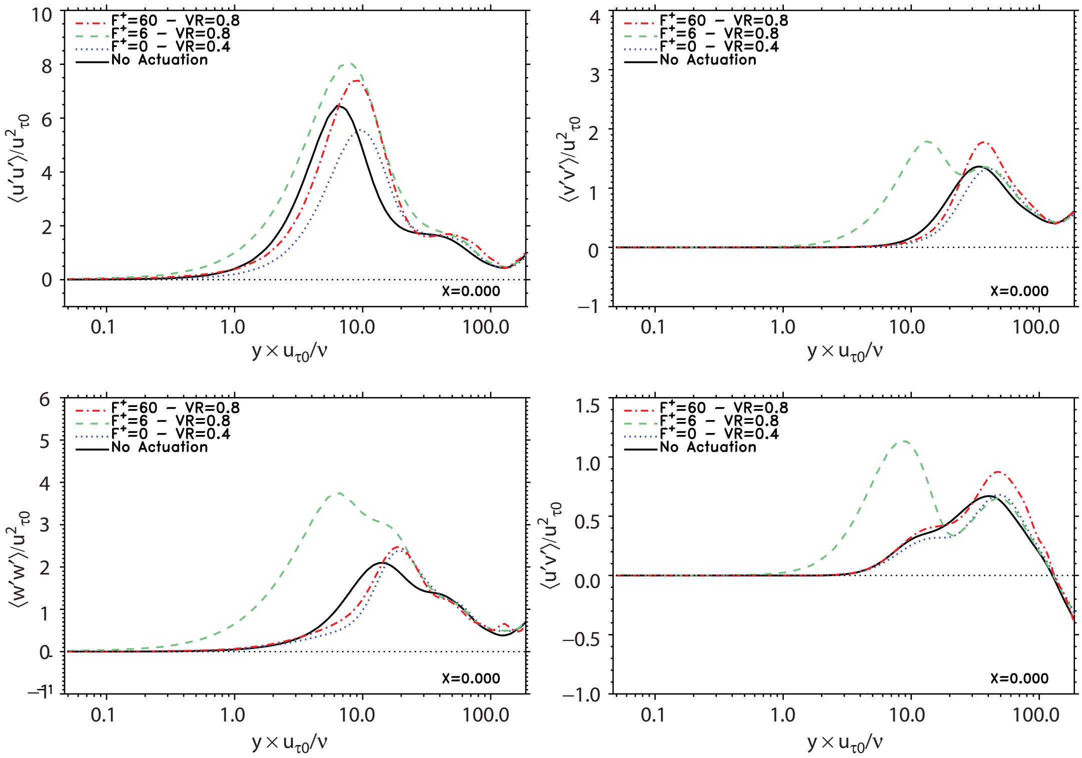

Figure 13: Influence of the frequency: Comparison of the spanwise-averaged Reynolds Stresses at $X = 0$, obtained for a control through S3 with FI=1% with three frequencies $F^+ = 0$, $F^+ = 6$ and $F^+ = 60$.

Farther downstream (Figure 14), the stresses start to recover the shape and level they would have had in the uncontrolled case, except for $F^+ = 6$. For the low pulsating frequency case, the levels of each stress is significantly reduced with respect to the other cases. This phenomenon can be easily explained by the fact that, because of the efficiency of the control at $F^+ = 6$, the flow is different from every other cases which are really close to each other.

To conclude, even for the lower mass-flux coming through the slot, the frequency has a real impact on the control efficiency. Moreover, the most effective frequency was found to be $F^+ = 6$ both for

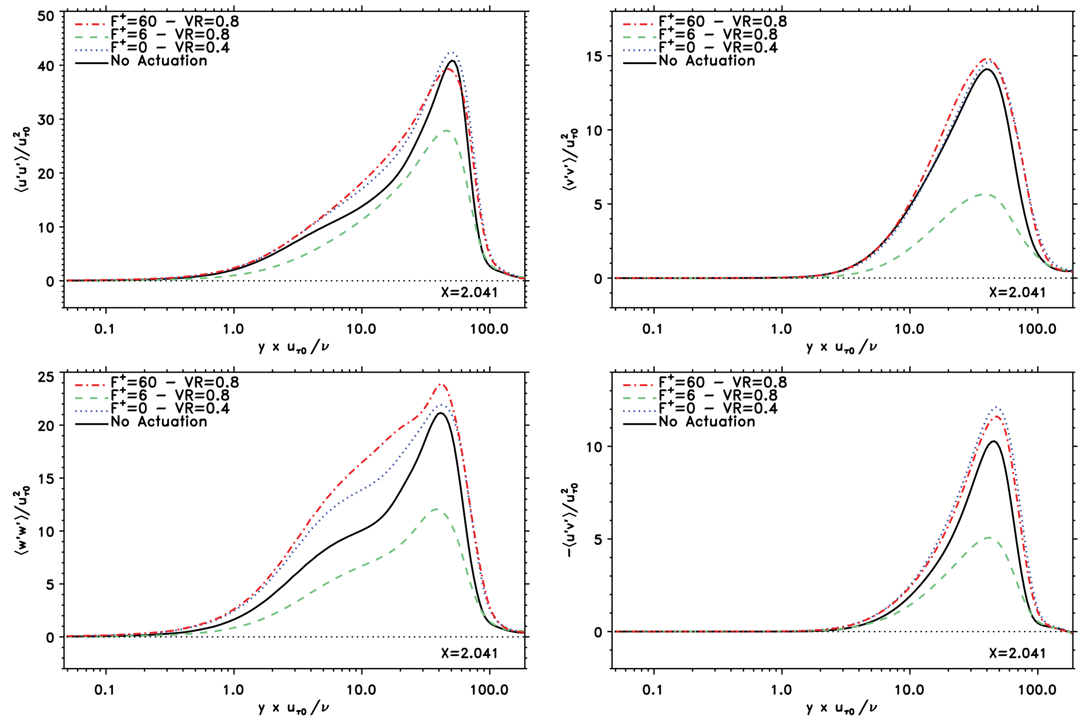

Figure 14: Influence of the frequency: Comparison of the spanwise-averaged Reynolds Stresses at X 2, obtained for a control through S3 with FI=1% with three frequencies $F^+ = 0$, $F^+ = 6$ and $F^+ = 60$.

reducing the boundary layer separation and for deeply modifying the flow. On the other hand, a high frequency does not yield any improvement with respect to a continuous blowing actuator.

A control with twice the mass-flux was then used to confirm the influence of the frequency. The shape of the separation bubbles, plotted in Figure 15, shows that, for such a control intensity, all the frequencies are able to at least modify the height of the bubble if not the length. However, a careful analysis of the friction coefficient (Figure 16) indicates that, unlike for the lower mass-flux, not only is the high frequency inefficient with respect to steady jets but it is even worse than the uncontrolled flow. The separation bubble is indeed around 66% longer than in the uncontrolled flow, which agrees with the results found by Dandois *et al*. [5]. This confirms the positive effect of low pulsating frequencies and the negative effect of high frequencies.

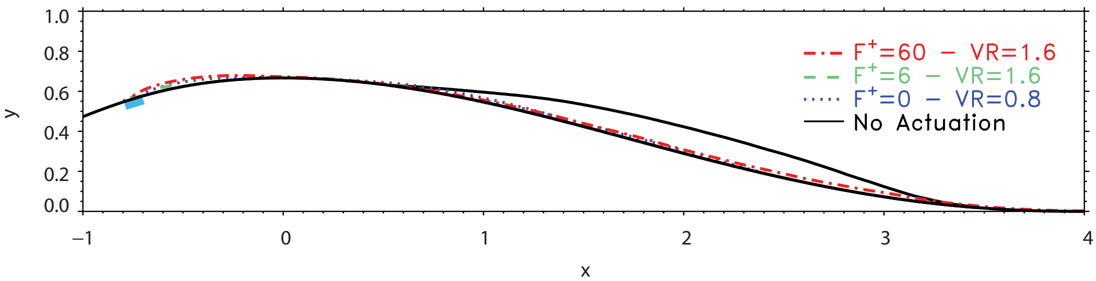

Figure 15: Influence of the frequency: comparison of the spanwise-averaged recirculation zones obtained for a control through S3 with FI=2% with three frequencies $F^+ = 0$, $F^+ = 6$ and $F^+ = 60$.

6.2. Influence of the jet amplitude

As it was previously shown in §5, the velocity ratio is an important parameter for the control. It is important since it defines the mass-flux coming through the slot, but also the stroke length of the jet and the energy involved. Moreover, this parameter can also be used as an input for closed-loop strategies. As a consequence, the influence of the *VR* is tested in this section for two different configurations, first for a steady blowing ($F^+ = 0$) and then for $F^+ = 6$.

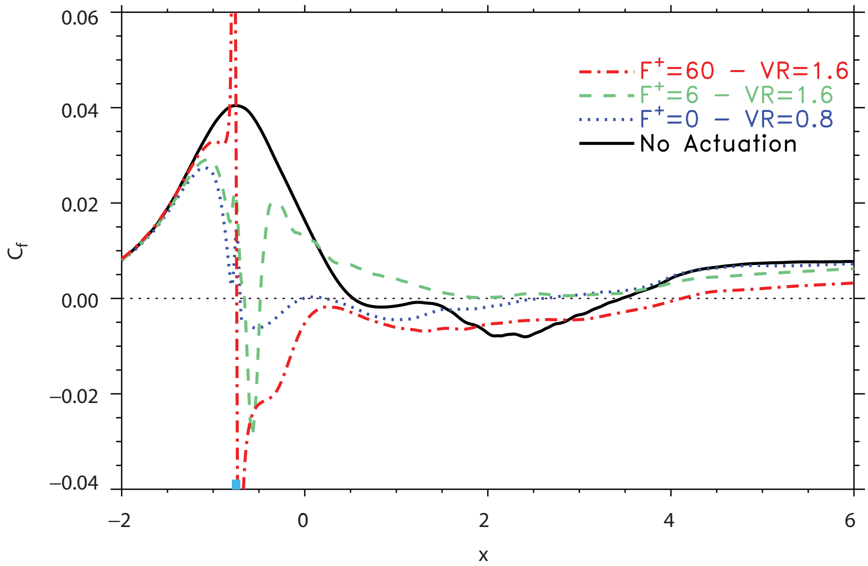

Figure 16: Influence of the frequency: streamwise evolution of the spanwise-averaged friction coefficient for a control through S3 with FI=2% with three frequencies $F^+ = 0$, $F^+ = 6$ and $F^+ = 60$.

Three different *VRs* are tested for the steady blowing case, $VR = 0.4$, $VR = 0.8$ and $VR = 1.6$, corresponding to a mass-flux of 1%, 2% and 4% of the incoming flow respectively. The separation bubbles are presented in Figure 17. It appears that the separating region in the diverging part of the bump is decreased from $VR = 0.4$ to $VR = 1.6$. On the other hand, this increase of the control intensity leads to a larger separation bubble in the immediate vicinity of the slot. Because of the steadiness of the control, the jet is observed to act as an obstacle for the cross-flow, creating a wake downstream of it. Thus, for $VR = 1.6$, and even if the boundary layer is attached throughout the diverging part of the bump, the separation bubble in the vicinity of the slot is too much a counterpart for the control to be considered as efficient. In addition, a larger increase of the control intensity would lead to a lower efficiency as the bubble in the wake of the jet would grow and eventually spread over the bump towards the diverging part. Therefore, the optimal control intensity is to be found between $VR = 0.8$ and $VR = 1.6$ for this kind of actuators. The streamwise evolution of the friction coefficient (Figure 18) shows that, in the diverging part of the bump, the friction coefficient reaches a plateau when increasing the control intensity, which level is increasing with *VR*.

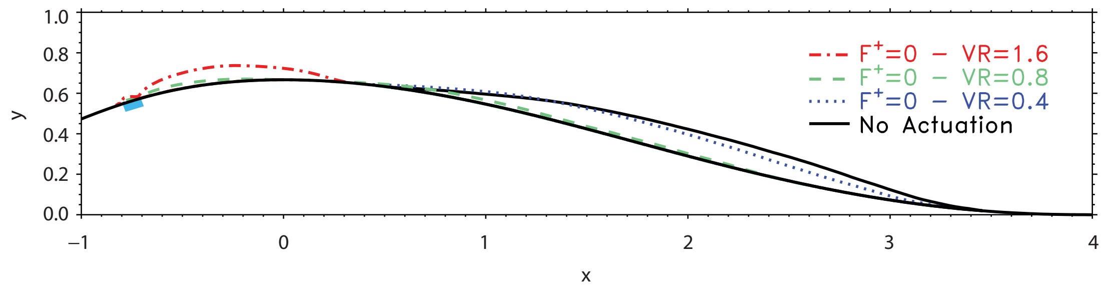

Figure 17: Influence of the jet amplitude: comparison of the spanwise-averaged recirculation zones obtained for a control through S3 at $F^+ = 0$ for $VR = 0.4$, $VR = 0.8$ and $VR = 1.6$.

The influence of the intensity on the Reynolds stresses (Figure 19-21) is then analysed. In the immediate neighbourhood of the slot (Figure 19), the peaks of $\langle v'v' \rangle$, $\langle w'w' \rangle$ and $\langle u'v' \rangle$ are moved away from the wall and their intensities are increased when increasing *VR*. Aside from those changes, the main shape of these stresses appears whatever the intensity. A new pattern however occurs for $\langle v'v' \rangle$ and $\langle w'w' \rangle$ at the highest intensity since a second peak appears for $VR = 1.6$, which is located closer to the wall than the main peak. For $\langle w'w' \rangle$, this peak occurs at the same location as the uncontrolled case, but is slightly moved towards the wall for $\langle v'v' \rangle$. A special attention has to be put

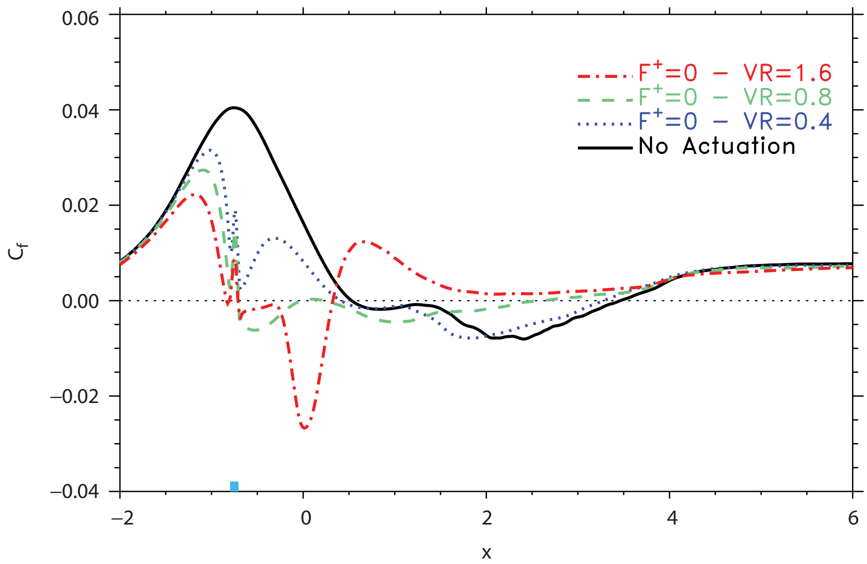

Figure 18: Influence of the jet amplitude: streamwise evolution of the spanwise-averaged friction coefficient obtained for a control through S3 at $F^+ = 0$ for $VR = 0.4$, $VR = 0.8$ and $VR = 1.6$.

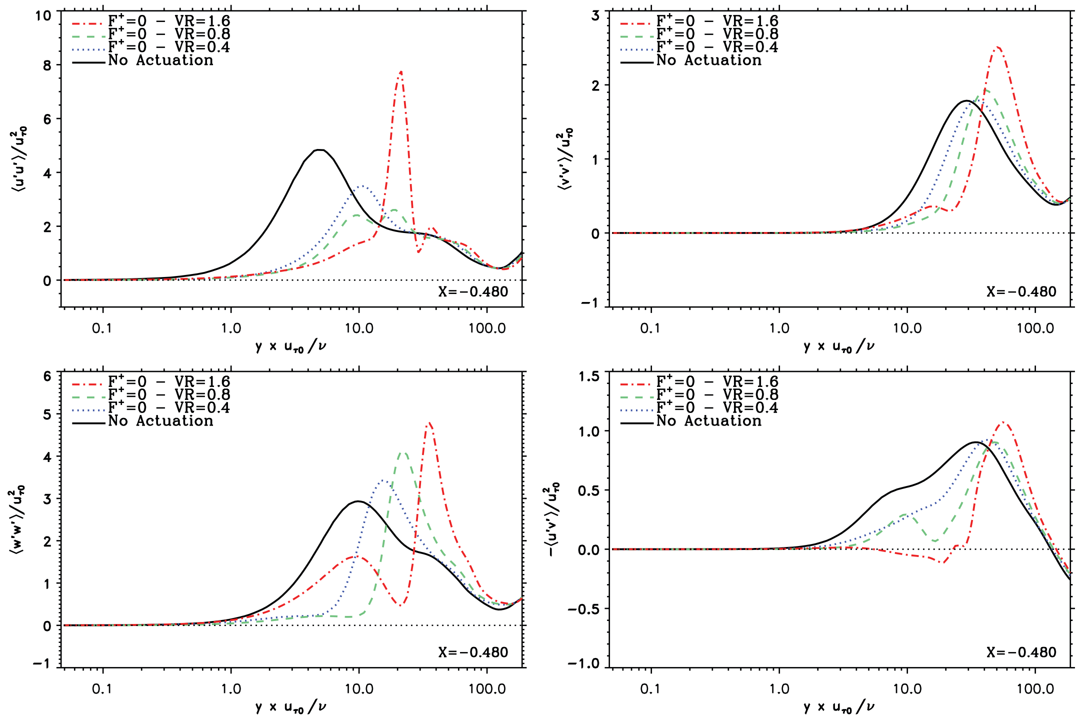

Figure 19: Influence of the jet amplitude: Comparison of the spanwise-averaged Reynolds Stresses at X −0.5, obtained for a control through S3 at $F^+ = 0$ for $VR = 0.4$, $VR = 0.8$ and $VR = 1.6$.

on $\langle u'u' \rangle$. Contrarily to the other normal stresses, the amplitude of the peak decreases when VR rises from $VR = 0.4$ to $VR = 0.8$ and then increases again for $VR = 1.6$. The sharp rise of the peak of $\langle u'u' \rangle$ for the highest VR and the greater distance from the wall at which it appears is due to the presence of a huge recirculation zone. Finally, it appears that even if they are different from each other, the profiles for VR = 0.8 and VR =1.6 both present a two-peak pattern. Concerning the shear stress $\langle u'v' \rangle$, the main modification occurs at VR =1.6 for which the stress is negative between y^+ 5 and y^+ 20. For this VR, The closest peak from the wall fades away and almost vanishes, while for $VR = 0.8$ the two peaks are recovered.

At the next position, corresponding to the top of the bump (Figure 20), it is obvious that the use of a higher control intensity leads to higher level for any stress throughout the boundary layer.

In addition, the boundary layer is modified over a larger wall-normal extent when using a larger control intensity.

Farther downstream (Figure 21), these trends evolve in the opposite way since higher velocity ratios lead to smaller turbulence intensities, as it was shown earlier.

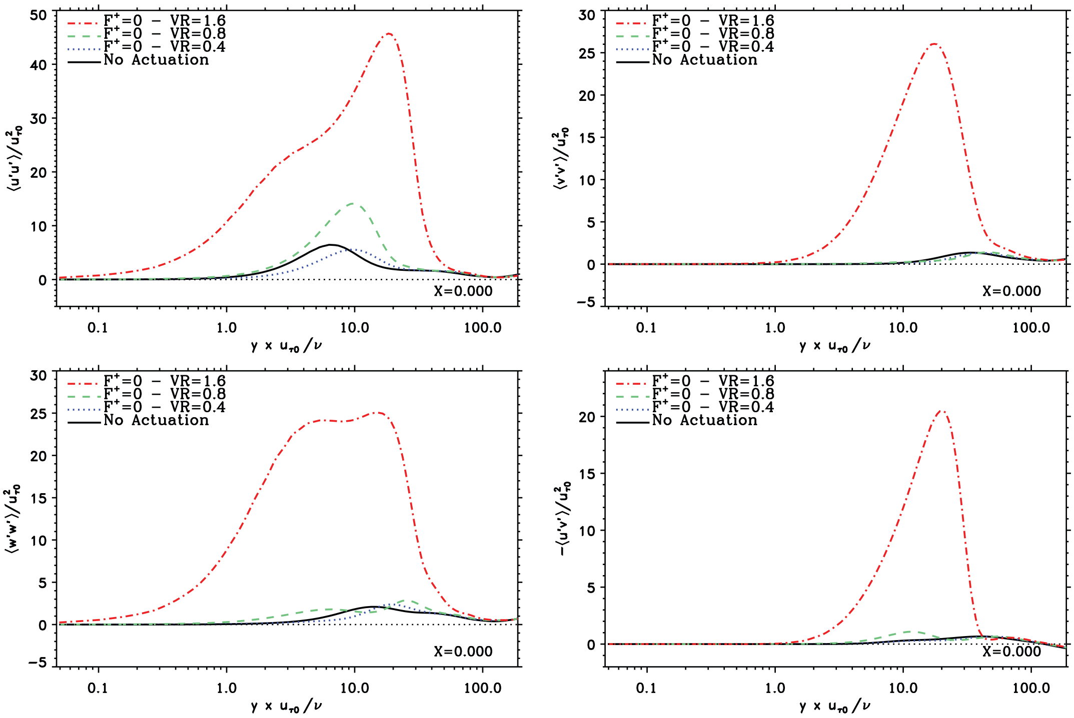

Figure 20: Influence of the jet amplitude: Comparison of the spanwise-averaged Reynolds Stresses at X = 0, obtained for a control through S3 at F^+ = 0 for VR = 0.4, VR = 0.8 and VR = 1.6.

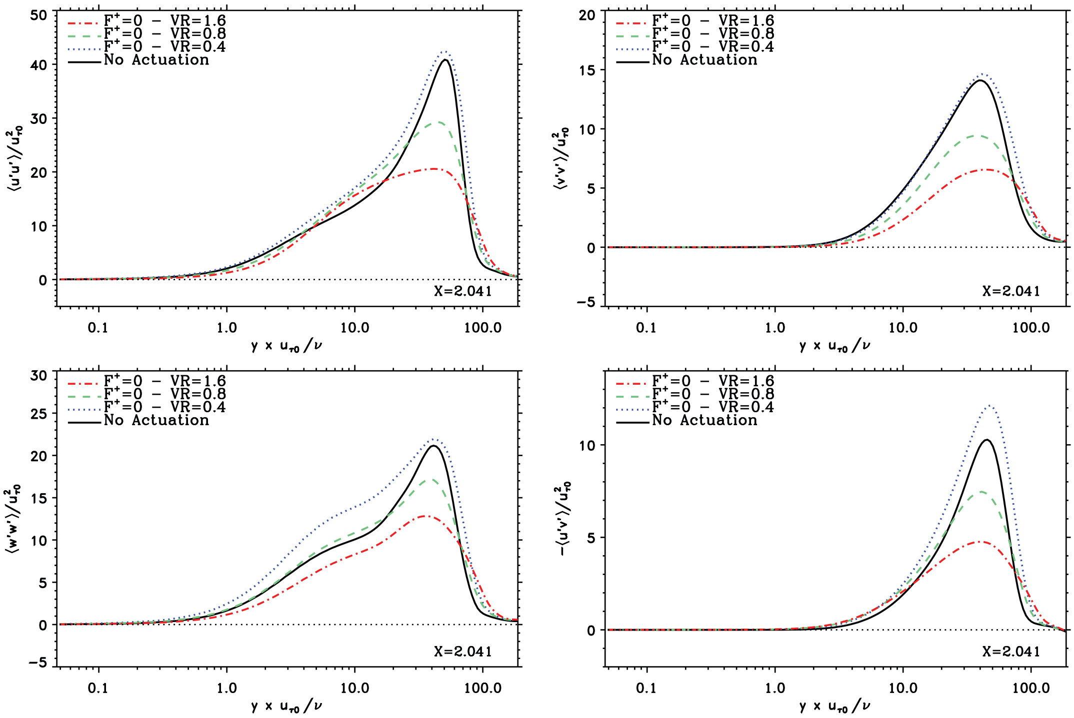

Figure 21: Influence of the jet amplitude: Comparison of the spanwise-averaged Reynolds Stresses at X 2, obtained for a control through S3 at F^+ = 0 for VR = 0.4, VR = 0.8 and VR = 1.6.

The low pulsating frequency $F^+ = 6$ is then considered for $VR = 0.8$, $VR = 1.6$ and $VR = 2.4$. Figure 22 displays the recirculation bubbles for the different cases. The results are improved when increasing VR. In addition, and even for the highest velocity ratio, the mean extent of the separation bubble in the wake of the actuator is drastically reduced as compared to the steady case. Concerning the friction coefficient (Figure 23), the increase of the plateau level with increasing VR in the diverging part, previously stated for the steady-jets actuator, is retrieved in the pulsed case, up to $VR = 1.6$. For the higher intensity ($VR = 2.4$), lower levels of the friction coefficient are found in the diverging part of the bump and C_f even reach negative values between X 1.25 and X 2.4. The boundary layer is therefore separated in this zone hence making the $VR = 2.4$ case less effective than $VR = 1.6$ for which the flow is attached. This observation thus allows to locate the optimal intensity for this pulsed-jet actuator between $VR = 0.8$ and $VR = 2.4$.

The modifications of the Reynolds stresses induced by an increase of the jet intensity are displayed in Figures 24-27. At $X = -0.5$ (Figure 24), the same conclusions as at $F^+ = 0$ can be drawn since the peaks of $\langle v'v' \rangle$, $\langle w'w' \rangle$ and $\langle u'v' \rangle$ are moved away from the wall and have their amplitude increased for a stronger control. Furthermore, the second peak that appears around $y^+ = 3$ on $\langle w'w' \rangle$ and which was already seen previously (Figure 12) has a slightly different behaviour since it is located closer to the wall and its magnitude increases with VR up to $VR = 1.6$ and then decreases for $VR = 2.4$. For $\langle u'u' \rangle$, the first peak, appearing around $y^+ = 11$ for $VR = 0.8$, behaves similarly to the other stresses and moves to $y^+ = 20$ and y^+ 30 for $VR = 1.6$ and $VR = 2.4$ respectively. On the other hand, and as for $\langle w'w' \rangle$, the second peak, closer to the wall, is slightly moved toward the wall up to $VR = 1.6$ and recovers its original position for $VR = 2.4$. Finally, it is noteworthy that the amplitude of the positive

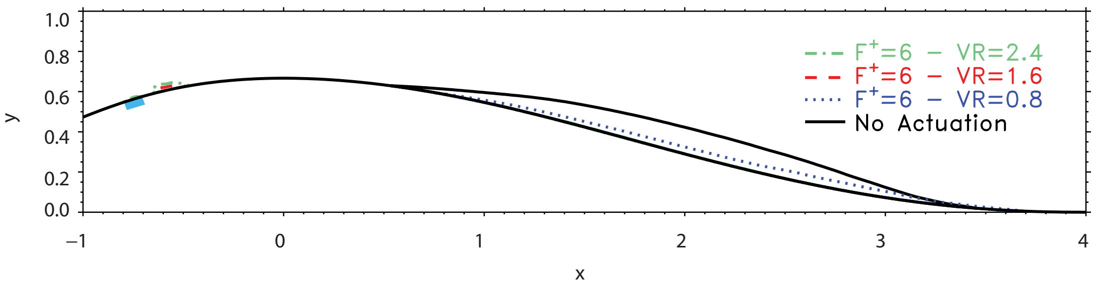

Figure 22: Influence of the jet amplitude: comparison of the spanwise-averaged recirculation zones obtained for a control through S3 at $F^+ = 6$ for $VR = 0.8$, $VR = 1.6$ and $VR = 2.4$.

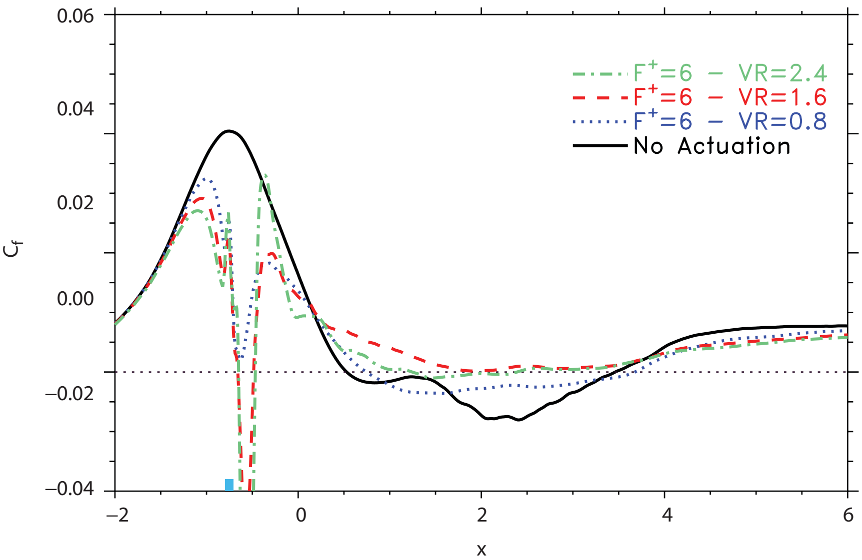

Figure 23: Influence of the jet amplitude: streamwise evolution of the spanwise-averaged friction coefficient obtained for a control through S3 at $F^+ = 2$ for $VR = 0.8$, $VR = 1.6$ and $VR = 2.4$.

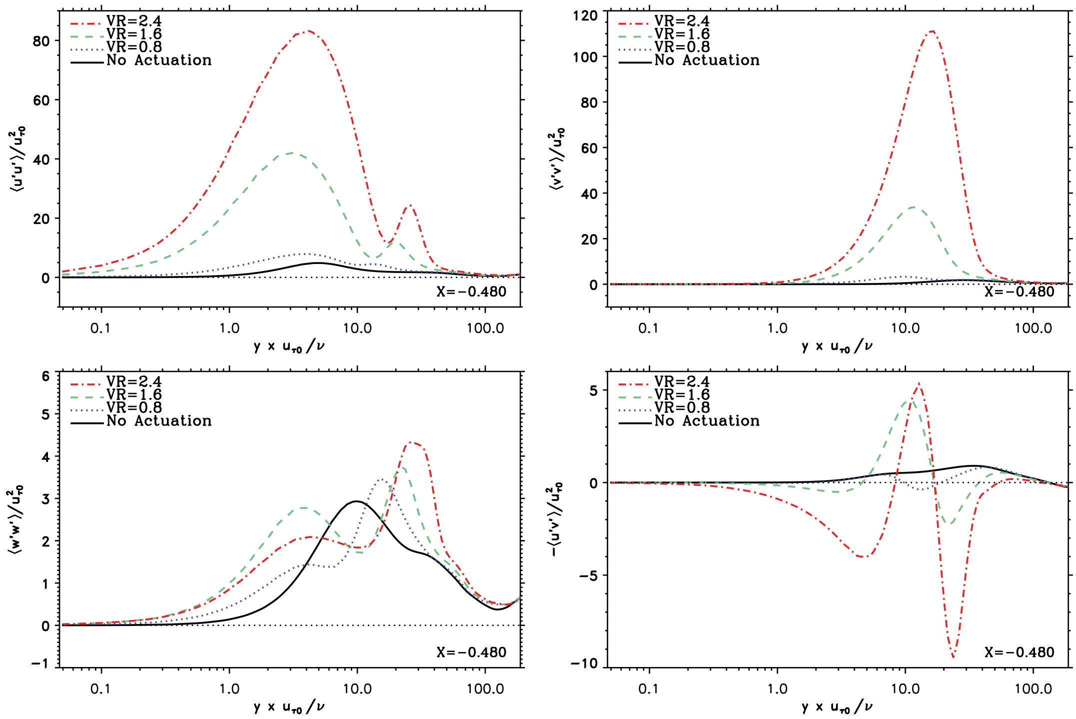

Figure 24: Influence of the jet amplitude: Comparison of the spanwise-averaged Reynolds Stresses at X −0.5, obtained for a control through S3 at $F^+ = 6$ for $VR = 0.8$, $VR = 1.6$ and $VR = 2.4$.

peaks on $\langle u'v' \rangle$ are only slightly modified between VR =1.6 and $VR = 2.4$, whereas the negative peaks are around five times more intense for the higher VR.

At the top of the bump (Figure 25), the same remarks as at the previous location can globally be made on both $\langle u'u' \rangle$ and $\langle v'v' \rangle$. However very different behaviours appear at $VR = 2.4$ on $\langle w'w' \rangle$ and $\langle u'v' \rangle$

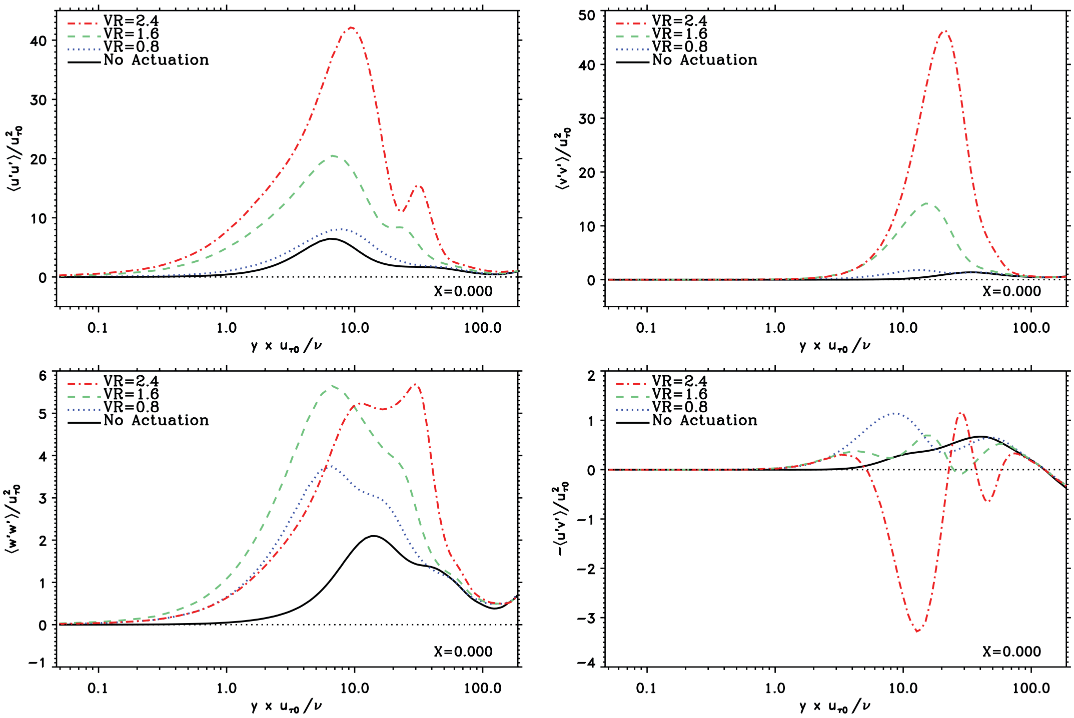

Figure 25: Influence of the jet amplitude: Comparison of the spanwise-averaged Reynolds Stresses at X = 0, obtained for a control through S3 at F^+ =6 for $VR = 0.8$, $VR = 1.6$ and $VR = 2.4$.

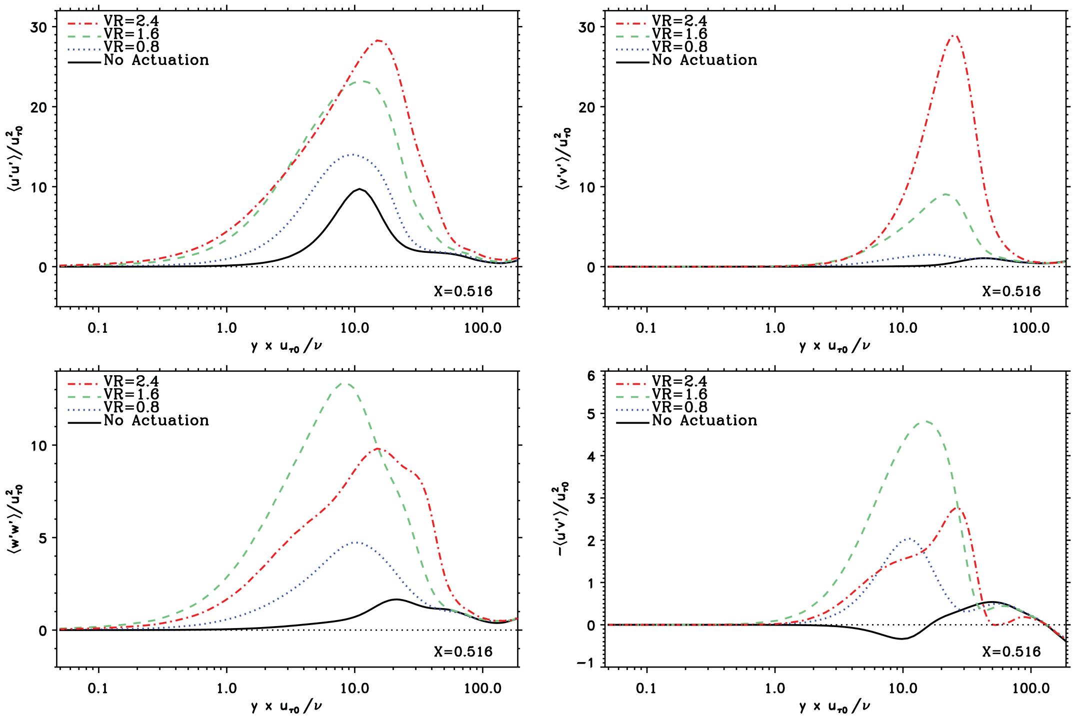

Figure 26: Influence of the jet amplitude: Comparison of the spanwise-averaged Reynolds Stresses at X 0.5, obtained for a control through S3 at $F^+ = 6$ for $VR = 0.8$, $VR = 1.6$ and $VR = 2.4$.

as compared to smaller VRs. First, the intensity of $\langle w'w' \rangle$ is not increased with respect to $VR = 1.6$. Moreover the two peaks, that are moved away from the wall, have almost the same intensity, which creates a small plateau of $\langle w'w' \rangle$ between $y^+ = 10$ and $y^+ = 30$. But the most modified stress happens to be the shear stress $\langle u'v' \rangle$. For this stress indeed, a new pattern occurs for each control intensity instead of being only dilated as it was the case just downstream of the slot (Figure 24). Hence for the weakest control ($VR = 0.8$), the profile presents an always-positive double peak-pattern, the maximum amplitude being reached around $y^+ = 9$ and $y^+ = 50$. When the applied control is two times larger ($VR = 1.6$), the two-peak profile evolves into a three-peak pattern. In addition, the stress encounters a change of sign between $y^+ = 25$ and $y^+ = 30$. Finally, for a further increased control intensity, the three-peak pattern still exists but now, $-\langle u'v' \rangle$ is negative for two zones, first between $y^+ = 5$ and $y^+ = 20$, then for $40 < y^+ < 60$.

At $X = 0.5$ (Figure 26), $\langle u'u' \rangle$ and $\langle v'v' \rangle$ still evolves accordingly, meaning that an increase of VR leads to an increase of the peaks magnitude and their displacement away from the wall. For $\langle w'w' \rangle$, the same increase of the control intensity up to VR =1.6 induces an increase of the peaks magnitude as well, however the peaks are now moved closer to the wall. A higher intensity ($VR = 2.4$) leads to the opposite evolution for both the intensity and the position of the peaks. The intensity is indeed decreased as compared to $VR = 1.6$, and the peak is moved away from the wall. Additionally, the profile has a totally different shape. At this position, the shear stress profile $-\langle u'v' \rangle$ recovers a behaviour similar to $\langle u'u' \rangle$ and $\langle v'v' \rangle$, at least up to $VR = 1.6$. The profile at $VR = 2.4$ is here again very different. If the main peak is moved away from the wall, and its intensity significantly decreases (almost two times smaller than for $VR = 1.6$), a second peak is discernible around $y^+ = 6$. In addition, the shear stress almost vanishes for $50 < y^+ < 60$.

At the next position, X 2, which corresponds to the last stage of the diverging part of the channel, the jet amplitude has only a weak influence on the stresses as compared to the previous locations. Hence, the stresses have almost the same shape whatever the VR. The only differences are seen on the amplitudes of the Reynolds stresses, which are slightly larger at $VR = 2.4$ than at $VR = 0.8$ and $VR = 1.6$. For those two lower VR, the statistics are almost identical.

This study about the influence of the jet amplitude at $F^+ = 6$ shed light on a very interesting aspect of the control. It is indeed noteworthy that in this case, the best results are not obtained when the Reynolds stresses are the most intense. It then tends to prove that introducing turbulent kinetic energy into the boundary layer along a wide streamwise extent is not a sufficient condition to efficiently control the flow separation.

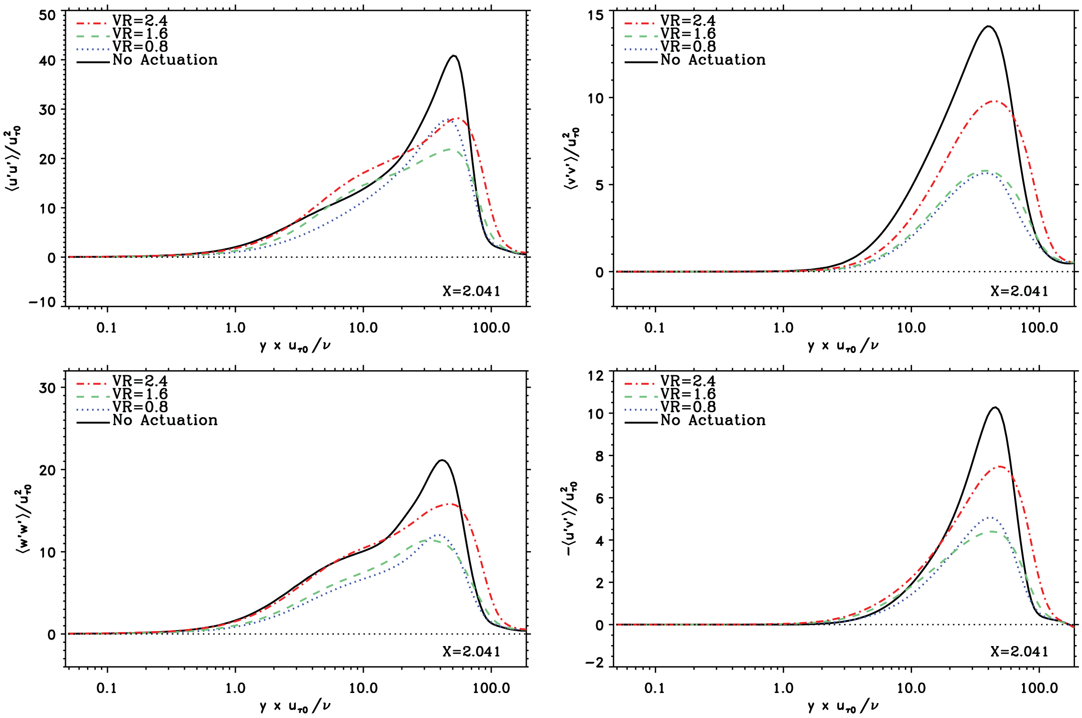

Figure 27: Influence of the jet amplitude: Comparison of the spanwise-averaged Reynolds Stresses at X 2, obtained for a control through S3 at $F^+ = 6$ for $VR = 0.8$, $VR = 1.6$ and $VR = 2.4$.

To conclude this section, it appears that the velocity ratio is an important parameter of the actuation. It is shown that, for a steady blowing, increasing the intensity of the control leads to a total suppression of the separation bubble in the diverging part of the channel. Nevertheless, the counterpart is that the wake of the jet grows with VR and enlarges the separation bubble in the immediate vicinity of the slot, leading to a reduced global efficiency of the control (see $VR = 1.6$). Moreover, higher VRs are expected to generate a larger bubble that would eventually extend downstream and spread throughout the diverging part of the channel. For pulsed jets, the same behaviour are observed up to $VR = 1.6$. For higher values of VR, the efficiency of the control decreases as the boundary layer starts to separate in the diverging part of the channel, as predicted from the steady case. Finally, it can be concluded that a control actuator cannot be efficient only by introducing turbulent kinetic energy into the boundary layer. The next section aims at understanding what are the mechanisms and the parameters linked to the control efficiency, and especially the role of the frequency.

7. PHYSICAL ANALYSIS

In order to complete the study performed in §6, an analysis of the vortical structures over the whole domain is carried out using both instantaneous fields and phase averages to identify what are the physical mechanisms that make $F^+ = 6$ more efficient than the other frequencies. The phase is taken in such a way that $\Phi = \pi$ and $\Phi = 2\pi$ are defined at the maximum actuation velocity and when the jets are turned off, respectively. $\Phi = \frac{\pi}{2}$ and $\Phi = \frac{3\pi}{2}$ correspond to the phase of increasing and decreasing blowing magnitude respectively (Figure 2).

7.1. Vortical structures

The vortical structures, represented by the Q-criterion ($Q = \frac{1}{2}\left(\Omega^2 - S^2\right)$ with Ω and S the vorticity and rate-of-strain tensors, respectively), are plotted for $F^+ = 0$, $F^+ = 6$ and $F^+ = 60$ in Figures 28, 29 and 30 respectively. In the continuous mode (Figure 28), as explained earlier, the jets act as an obstacle for the surrounding flow. As a result, a shear layer appears in the form of sheets of Q-criterion, that tear into large spots of vorticity. These highly three-dimensional structures have an extent of several tens of slot width in both streamwise and spanwise directions. In addition, their shedding does not seem to occur at a unique frequency but rather in a broad range of frequencies.

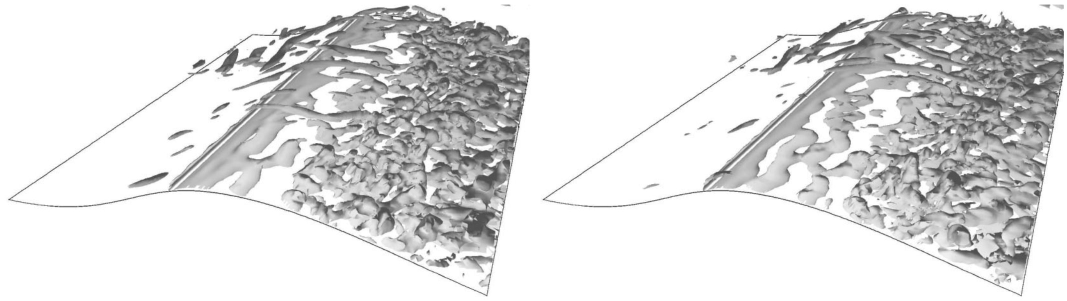

Figure 28: Isosurfaces of the Q-criterion obtained for a control through S3 at $F^+ = 0$ for $VR = 0.8$ at $T = 41.0$ and $T = 41.6$

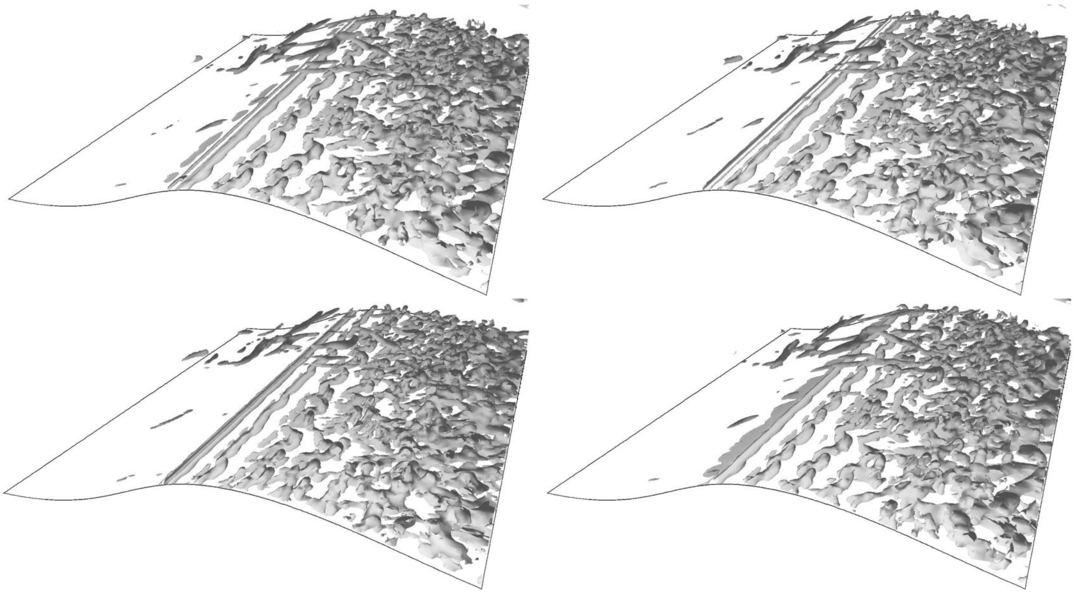

Figure 29: Isosurfaces of the Q-criterion obtained for a control through S3 at $F^+ = 6$ for $VR = 0.8$ at $\Phi = \frac{\pi}{2}, \Phi = \pi, \Phi = \frac{3\pi}{2}$ and $\Phi = 2\pi$.

When applying a low-frequency control $F^+ = 6$ (Figure 29), a different behaviour is observed. Under the influence of the increasing jet ($\Phi = \pi/2$), a vortical quasi-2D tube is created in the immediate vicinity of the slot. This structure grows up to a diameter of a few slot widths, until the jet reaches its maximum amplitude ($\Phi = \pi$) and is shed when the jet amplitude starts to decrease. The vortices are then convected by the cross-flow while the blowing intensity is diminishing ($\Phi = 3\pi/2$), turning into 3D structures through a 3D instability. They then evolve into an array of hairpin vortices, that will eventually collide and mix with the shear layer structures farther downstream. Meanwhile a new structure is created close to the slot and will undergo the same evolution and so on. Two important observations can be made for this low-frequency case. First, the shedding frequency is exactly synchronised with the jet frequency. In addition, a spanwise wavelength clearly appears on the vortical structures shed in the wake of the jet. This wavelength was found to be λ_z 0.6, which corresponds to approximatively 7 slot widths, or 110 wall-units at the inlet (that is more or less the streaks spacing in a ZPG boundary layer [15]). Therefore, it can be conclude that a low-frequency control induces a more coherent organisation in the flow structures, with smaller and more regular vortices as compared to the steady case.

The vortical structures obtained for a high-frequency control ($F^+ = 60$) are displayed in Figure 30 when the actuation is at its maximum ($\Phi = \pi$) and when it is turned off ($\Phi = 2\pi$). It appears that the vortices have a shape comparable to the steady case, with nonetheless some slight differences. First, even if the sheet-pattern of the structures is recovered, the sheet of Q-criterion is smoother and more regular than at $F^+ = 0$. It also appears that the sheets spread over a larger streamwise extent prior to be torn apart. In addition, the shed structures are smaller and most of them disappear just after being shed.

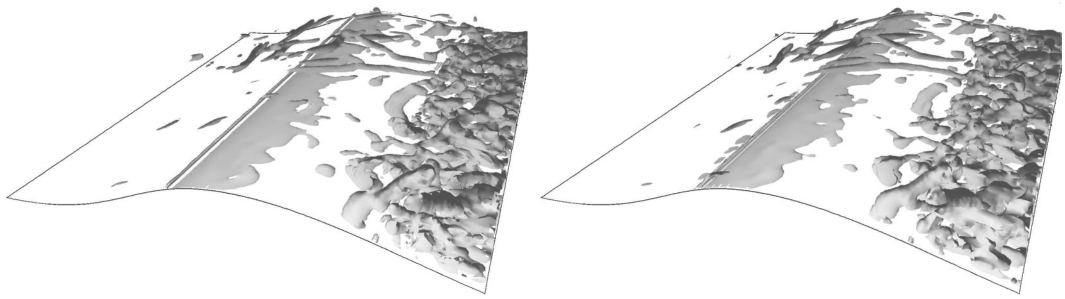

Figure 30: Isosurfaces of the Q-criterion obtained for a control through S3 at $F^+ = 60$ for $VR = 0.8$ at $\Phi = \pi$ and $\Phi = 2\pi$.

The vanishing of the shed vortices is the reason that can explain the large zone with almost no structures that occurs only for $F^+ = 60$, before a large amount of vortices is created again but of larger size and with a different organisation than in the previous two cases. Finally, a slight flapping of the sheet's downstream boundary is visible, suggesting that, in spite of the absence of regular shedding, as for $F^+ = 6$, the jet frequency has an impact on the created vortices.

As a conclusion, the efficiency of the low-frequency control is closely related to the shedding of quasi-2D vortices in the immediate vicinity of the slot, synchronised with the jet frequency, that does not occur for the steady case and at higher frequencies. When convected downstream, these very regular structures are then stretched and distorted -until they finally take the shape of spanwise lines of hairpin vortices with a spanwise wavelength of around 7 slot widths, resulting in a highly organised motion downstream of the slot, as compared to the other cases.

7.2. Phase average

The phase (and spanwise) averages, plotted in Figure 31, are also a good representation to understand what happens during a single period of actuation. Four different phases are considered for the low-frequency control, corresponding to an increasing actuation ($\Phi = \pi/2$), the maximum blowing ($\Phi = \pi$),

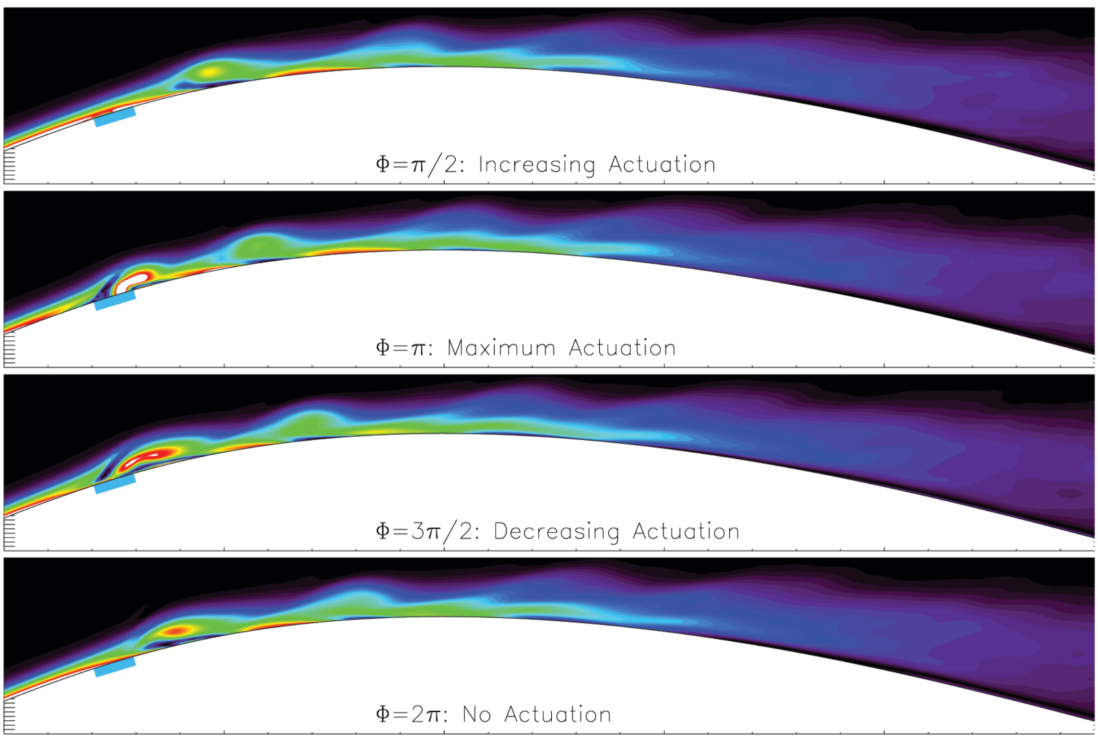

Figure 31: Phase- and spanwise-averaged spanwise vorticity obtained for a control through S3 at $F^+ = 6$ for $VR = 0.8$ at $\Phi = \frac{\pi}{2}$, $\Phi = \pi$ and $\Phi = \frac{3\pi}{2}$ and $\Phi = 2\pi$.

a decreasing actuation $\Phi = 3\pi/2$ and no actuation ($\Phi = 2\pi$). As stated by Avdis *et al*. [3] and confirmed by the present study, the specific time variation of the control leads to the periodic creation of spanwise structures according to the following process. During the increasing part of the control ($\Phi = \pi/2$), the fluid close to the wall, that is attached at the slot position when the control is off, progressively separates and rolls up to create a spanwise structure in the immediate vicinity of the slot ($\Phi = \pi$). This structure is then shed when the actuation intensity starts to decrease and is advected by the cross-flow ($\Phi = 3\pi/2$). Under the influence of the favourable pressure gradient created by the converging part of the bump, the vortices are constricted and accelerated and their intensity progressively decrease. They eventually lose their circular shape and mix with the structures that occur in the boundary layer farther downstream. Because of their clockwise rotation, these regularly shed spanwise vortices are able to move some fluid towards the wall and increase the velocity in the boundary layer, therefore preventing the separation.

One of the most interesting observations, made both on the instantaneous structures and on the phase averages is that the generation of spanwise vortices, leading to a reattached boundary layer, occurs during the increasing phase of the jet amplitude. In addition, and because these structures disappear in the steady case, the decreasing part has a great importance since it is responsible for the vortex shedding. However, the inefficiency of the high-frequency case $F^+ = 60$ demonstrates that having these two features is not a sufficient condition. In conclusion, it can be said that the vortex shedding and the subsequent improvement on the global efficiency of the control are obtained only if the increasing stage of blowing, that entrains fluid in its wake, lasts long enough for a vortex to be created.

8. CONCLUSIONS

The control of the flow in a converging/diverging channel by means of a spanwise slot was studied using Direct Numerical Simulations and Large-Eddy Simulations. In the first part, DNS was performed for a steady, normal-to-the-wall blowing actuator in order to calibrate the efficiency of such a control. It was shown that under certain conditions, particularly the position of the actuator, the separation bubble appearing in the divergent part of the channel in the uncontrolled case can be entirely suppressed by a steady control. The LES part of the code has then been validated for both uncontrolled and controlled cases in §4. LES shows a very good agreement with DNS in the uncontrolled case and only slight differences appear when a blowing is applied. LES was then used to analyse the influence of the frequency and intensity of the wall-normal jets on the control efficiency (§6). A reduced frequency of $F^+ = 6$ was demonstrated to lead both to an attached boundary layer throughout the diverging part, and to the greatest modifications of the flow, and particularly of the Reynolds stresses. It was also shown that increasing the control intensity can be of negative effect on the global efficiency. Finally, an analysis of the vortical structures was proposed in §7. A very different flow organisation is evidenced for $F^+ = 6$ that does not appear for the other test cases. At this particular frequency, spanwise vortices are regularly shed in the wake of the actuator jet. They have a spanwise spacing of the order of the incoming boundary layer streaks spacing and evolve quickly to hairpin vortices that increase the three-dimensionality of the flow in that part of the bump. This leads us to think that it is the streaks instability which is excited at this frequency. On the other hand, for steady blowing and high frequency actuation, no clear vortex shedding occurs and the vorticity is very irregularly created by the control.

9. ACKNOWLEDGEMENTS

The authors would like to thank CISIT (International Campus on Safety and Intermodality in Transport) for its financial support and the computing facilities of Lille University (CRI) and IDRIS (French CNRS National Computing Facilities) for the CPU time on their facilities. The authors are grateful to Matthieu Marquillie for his help with the numerical code.

9. REFERENCES

[1] Amitay, M., and Cannelle, F. Evolution of finite span synthetic jets. *Physics of Fluids 18* (2006), 054101–1 054101–16.

[2] Amitay, M., and Glezer, A. Flow transients induced on a 2D airfoil by pulse-modulated actuation. *Experiments in Fluids 40* (2006), 329-331.

[3] Avdis, A., Lardeau, S., and Leschziner, M. Large eddy simulations of separated flow over a two-dimensional hump with and without control by means of a synthetic slot-jet. *Flow Turbulence and Combustion 83* (2009), 343–370.

[4] C. Cierpka, Weier, T., and Gerbeth, G. Synchronized force and particle image velocimetry measurements on a naca 0015 in poststall under control of time periodic electromagnetic forcing. *Physics of Fluids 22* (2010), 075109.

[5] Dandois, J., Garnier, E., and Sagaut, P. Numerical simulation of active separation control by a synthetic jet. *Journal of Fluid Mechanics 574* (2007), 25–58.

[6] Gad-EL-Hak, M. *Flow Control: passive, active and reactive flow management*. Cambridge University Press, 2000.

[7] Glezer, A., and Amitay, M. Synthetic jets. *Annual Reviews of Fluid Mechanics 34* (2002), 503–529.

[8] Godard, G., and Stanislas, M. Control of a decelerating boundary layer. part 1: Optimization of passive vortex generators. *Aerospace Science and Technology 10* (2006), 181-191.

[9] Greenblatt, D., Paschal, K. B., Yao, C., and Harris, J. Experimental Investigation of Separation Control Part 2: Zero Mass-Flux Oscillatory Blowing. *AIAA Journal 44* (2006), 2831–2845.

[10] Greenblatt, D., and Wygnanski, I. J. The control of flow separation by periodic excitation. *Progress in Aerospace Science 36* (2000), 487–545.

[11] Kostas, J., Foucaut, J., and Stanislas, M. The flow structure produced by pulsed-jet vortex generators in a turbulent boundary layer in an adverse pressure gradient. *Flow, Turbulence and Combustion: Special Issue on Air-jet Actuators and Their Use for Flow Control 78,* 3–4 (2007), 331–363.

[12] Kostas, J., Foucaut, J., and Stanislas, M. The effects of pulse frequency and duty cycle on the skin friction downstream of pulsed jet vortex generators in an adverse pressure gradient turbulent boundary layer. *Aerospace Science and Technology 13* (2009), 36–48.

[13] Laval, J.-P., Braud, C., Fournier, G., and Stanislas, M. Large-eddy simulations of control of a separated flow over a 2d bump by means of pulsed jets. *Journal of Turbulence 11,* 52 (2010), 1–33.

[14] Laval, J.-P., Elsner, W., Kuban, L., and Marquillie, M. LES modeling of converging diverging turbulent channel flow. In *Progress in wall turbulence: understanding and modeling,* M. Stanislas, J. Jimenéz, and I. Marusic, Eds., ERCOFTAC Series. Springer, April 21-23 2010, pp. 355–363.

[15] Lin, J., Laval, J.-P., Foucaut, J.-M., and Stanislas, M. Quantitative characterization of coherent structures in the buffer layer of near-wall turbulence. Part 1: Streaks. *Experiments in Fluids 45,* 6 (2008), 999–1013.

[16] Lin, J. C. Review of research on low-profile vortex generators to control boundary-layer separation. *Progress in Aerospace Science 38* (2002), 389-420.

[17] Lumley, J., and Blossey, P. Control of Turbulence. *Annual Review of Fluid Mechanics 30* (1998), 311–327.

[18] Marquillie, M., Ehrenstein, U., and Laval, J.-P. Instability of streaks in wall turbulence with adverse pressure gradient. *Journal of Fluid Mechanics*, in press, available online (DOI:10.1017/jf.2011.193) (2010).

[19] Marquillie, M., Laval, J.-P., and Dolganov, R. Direct numerical simulation of a separated channel flow with a smooth profile. *Journal of Turbulence 9,* 1 (2008), 1–23.

[20] Nicoud, F., and Ducros, F. Subgrid-scale stress modeling based on the square of the velocity gradient tensor. *Flow, Turbulence and Combustion 62* (1999), 193–200.

[21] Roth, J. R. Aerodynamic flow acceleration using paraelectric and peristaltic electrohydrodynamic effects of a one atmosphere uniform glow discharge plasma. *Physics of Plasmas 10* (2003).

[22] Roth, J. R., Sherman, D. M., and Wilkinson, S. P. Electrohydrodynamic flow control with a glow-discharge surface plasma. *AIAA Journal 38,* 7 (2000), 1166–1172.

[23] Seifert, A., Bachar, T., Koss, D., Shepshelovich, M., and Wygnanski, I. Oscillatory blowing: a tool to delay boundary-layer separation. *AIAA Journal 31,* 11 (1993), 2052–2060.

[24] Tilmann, C., Langan, K. L., Betterton, J., AND Wilson, M. Characterization of pulsed vortex generator jets for active flow control. In *RTO AVT Symposium on "Active Control Technology for Enhanced Performance Operational Capabilities of Military Aircraft, Land Vehicles and Sea Vehicles* (Germany, 2000).